

2007

Investigation of an energy harvesting small unmanned air vehicle

Kyle Christopher Magoteaux
University of Dayton

Follow this and additional works at: https://ecommons.udayton.edu/graduate_theses

Recommended Citation

Magoteaux, Kyle Christopher, "Investigation of an energy harvesting small unmanned air vehicle" (2007).
Graduate Theses and Dissertations. 4129.
https://ecommons.udayton.edu/graduate_theses/4129

This Thesis is brought to you for free and open access by the Theses and Dissertations at eCommons. It has been accepted for inclusion in Graduate Theses and Dissertations by an authorized administrator of eCommons. For more information, please contact mschlangen1@udayton.edu, ecommons@udayton.edu.

**Investigation of an Energy Harvesting Small Unmanned
Air Vehicle**

Thesis

Submitted to

The School of Engineering of the
UNIVERSITY OF DAYTON

in Partial Fulfillment of the Requirements for

The Degree

Master of Science in Aerospace Engineering

by

Kyle Christopher Magoteaux

UNIVERSITY OF DAYTON

Dayton, Ohio

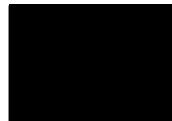
December, 2007

Investigation of an Energy Harvesting Small Unmanned Air Vehicle

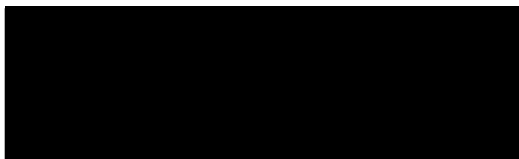
APPROVED BY:



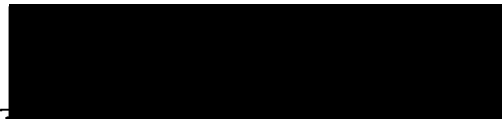
Brian Sanders, Ph.D.
Advisory Committee Chairman
Adjunct Professor, Department of
Mechanical & Aerospace Engineering



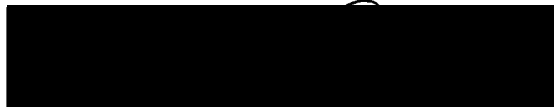
Kevin Hallinan, Ph.D.
Committee Member
Chairperson, Department of
Mechanical & Aerospace Engineering



Michael L. Turner, Ph.D.
Committee Member
Assistant Professor, Department of
Mechanical & Aerospace Engineering



Malcolm W. Daniels, Ph.D.
Associate Dean
School of Engineering



Joseph E. Saliba, Ph.D., P.E.
Dean, School of Engineering

ABSTRACT

Investigation of an Energy Harvesting Small Unmanned Air Vehicle

Name: Magoteaux, Kyle Christopher

University of Dayton, 2007

Advisor: Brian Sanders, Ph.D.

In this thesis the addition of energy harvesting is investigated to determine the benefits of integrating it into a small unmanned air vehicle (UAV). Specifically, solar and mechanical energy harvesting techniques were selected and their basic functions analyzed. The initial investigation involved using a fundamental law of thermodynamics, entropy generation, to analyze both the small UAV with and without energy harvesting. A notional reconnaissance mission was developed for the comparison of the aircrafts. This analysis showed that while the UAV with energy harvesting generated less entropy, the UAV without energy harvesting outperformed the other UAV in total flight time at the target. The analysis further looked at future energy harvesting technologies and their effect on the energy harvesting UAV. The analysis showed that with these advanced technologies energy harvesting would increase the effectiveness of the energy harvesting vehicle making it possible to outperform the UAV without energy harvesting. Additionally, both the solar and piezoelectric technologies were characterized experimentally and analytically. With this information, designs for integrating energy harvesting into the small UAV system were developed and tests were conducted to show how the energy harvesting designs would

perform. It was demonstrated that the addition of the solar and piezoelectric devices would supply usable power for charging batteries and sensors and that it would be advantageous to implement them into a small UAV.

Acknowledgements

I would like to thank my wife Sarah Jane for giving the support and love I needed to complete my time in graduate school. I would like to thank Brian Sanders for the opportunity to conduct this research and for advising me throughout the duration of my research. Additionally, a thank you goes to Kevin Hallinan, Michael Turner, Jason Bowman, and Robin McCarty for providing their knowledge and technical support.

Contents

Chapter	
1	Introduction 1
1.1	Motivation 1
1.2	Small Unmanned Air Vehicles 2
1.3	Energy Harvesting 3
1.4	Problem Statement 4
2	Background 7
2.1	Solar Technology 7
2.1.1	Basic Principles of Solar Technology 8
2.1.2	Solar Cell Applications 9
2.2	Piezoelectric Technology 13
2.2.1	Basic Principles of Piezoelectric Technology 13
2.2.2	Piezoelectric Applications 14
2.3	Thermodynamic Analysis 15
2.4	Chapter Summary 16
3	Entropy Generation Analysis 18
3.1	Entropy Generation 18
3.1.1	Calculating Entropy Generation 19

3.1.2	Control Volume Selection	19
3.2	Mission Simulation	32
3.2.1	Mission Definition	32
3.2.2	Aerodynamic Analysis	36
3.2.3	Mission Simulation Results	38
3.3	Conclusions	47
4	Energy Harvesting Characterization	49
4.1	Solar Technology	49
4.1.1	Solar Cell Characterization	50
4.2	Piezoelectric Technology	54
4.2.1	Piezoelectric Beam Characterization	54
4.3	Chapter Summary	58
5	Energy Harvesting Integration	62
5.1	Solar Harvesting	62
5.2	Mechanical Vibration Harvesting	68
5.2.1	Cantilevered Landing Gear	69
5.2.2	Curved Beam Landing Gear	72
5.3	Conclusions	76
6	Conclusions and Recommendations	79
6.1	Energy Harvesting for Small UAVs	79
6.2	Recommendations	81
 Appendix		
A	Entropy Generation	82

A.1 Aircraft Control Volumes	82
B Additional Solar Cell Characterizations and Battery Charging Tests	84
Bibliography	88

Figures

Figure

1.1	AeroVironment Black Widow [1]	2
1.2	Proposed Solution to Small UAV Energy Needs	5
2.1	The Solar P-N Junction [2]	8
2.2	Equivalent Circuit of a Solar Cell [3]	9
2.3	A Solar Cell Being Struck by Light [4]	10
2.4	Camel Carrying Refrigeration Unit [3]	12
2.5	Poling Process for Synthetic Piezoelectric Materials [5]	14
3.1	RC Aircraft Used in Analysis	20
3.2	Control Volume for Micro Stick Aircraft	21
3.3	Illustration of Operational Entropy	22
3.4	Total Entropy Generated vs. Battery Efficiency and Controller Efficiency . .	28
3.5	Total Entropy Generated vs. Battery Efficiency and Motor Efficiency	29
3.6	Total Entropy Generated vs. Battery Efficiency and Propeller Efficiency . .	31
3.7	Total Entropy Generated vs. Motor Efficiency and Propeller Efficiency . . .	31
3.8	Control Volume for EH Aircraft	33
3.9	Base Aircraft Mission Illustration	35
3.10	EH Aircraft Mission Illustration	35

3.11 S_{gen} Accounting for Solar Cell	39
3.12 S_{gen} for Entire Mission	40
3.13 S_{gen} for EH Aircraft over Entire Mission	40
3.14 Total S_{gen} for Base Aircraft Mission	41
3.15 S_{gen} for Dash Segment of Mission	43
3.16 S_{gen} for Loiter Segment of Mission	43
3.17 Total Loiter Time at Target Location	44
3.18 Total Loiter Time at Target Location 1 Mile Away for Increasing Efficiencies	46
3.19 Total Loiter Time at Target Location 1 Mile Away for Monocrystalline and Amorphous Solar Cells	46
3.20 S_{gen} for Dash Segment of Mission for Monocrystalline and Amorphous Solar Cells	48
3.21 S_{gen} for Loiter Segment of Mission for Monocrystalline and Amorphous Solar Cells	48
4.1 Daystar Solar Meter Used in Solar Cell Characterization	51
4.2 Test Setup for Solar Cell Characterization	51
4.3 Monocrystalline Solar Cell Characterization on August 17th	52
4.4 Amorphous Solar Cell Characterization on August 17th	52
4.5 Piezo Systems, Inc. Standard Quick-Mount Bending Generator, P/N Q220- A4-103YB	57
4.6 Frequency Response From the Experiment Compared to the Analytical Model	59
4.7 Voltage Output of the Beam Generator at 295 Hz across a 17.4 k Ω Resistor	59
4.8 Current Output of the Beam Generator at 295 Hz across a 17.4 k Ω Resistor	60
5.1 Flexible Amorphous Solar Cell	63
5.2 Amorphous Solar Cells Conforming to Airfoil	64

5.3	Maxim Integrated Products MAX745EVKIT Switch Mode Lithium Ion Battery Charging Circuit [6]	64
5.4	Test Setup for Charging Batteries	65
5.5	Battery Charging Starting at 8:30 a.m. on July 10th and Restarted on July 12th at 9:00 a.m. Due to Inclement Weather	66
5.6	Battery Charging Starting at 8:30 a.m. on August 1st Showing 2 Discharges	67
5.7	Initial Design for Piezoelectric Generators Inside Wing Structure	68
5.8	Illustration of Cantilevered Piezoelectric Beam Used as Landing Gear . . .	69
5.9	Frequency Response of Piezo Systems Beam	70
5.10	Natural Frequency of Modeled Beam with 75 gram Tip Mass	71
5.11	Power Output of Modeled Beam with 75 gram Tip Mass	71
5.12	Natural Frequency of Modeled Beam with 25 gram Tip Mass	73
5.13	Power Output of Modeled Beam with 25 gram Tip Mass	73
5.14	Illustration of Curved Piezoelectric Beam Used as Landing Gear	74
5.15	Face International Corporation Thunder [®] Actuator TH-8R Curved Beam .	74
5.16	Test Setup for Curved Beam Landing Gear	74
5.17	Closeup of Curved Beam Landing Gear	75
5.18	Curved Beam Output at 5.5 m/s ² for Two Simulated Aircraft Masses	76
5.19	Curved Beam Output at 10 m/s ² for Two Simulated Aircraft Masses	77
5.20	Maximum Power Outputs at Natural Frequency of Model Landing Gear . . .	77
A.1	Control Volume With Detailed Work and Heat Rates	83
A.2	Energy Harvesting Additions	83
B.1	Solar Cell Characterization for Powerfilm [®] MP3-37 on May 24th	85
B.2	Solar Cell Characterization for Powerfilm [®] SP4.2-37 on May 24th	85
B.3	Solar Cell Characterization for Powerfilm [®] MPT4.8-75 on May 24th	86

B.4	Solar Cell Characterization for Powerfilm® MPT15-75 on May 24th	86
B.5	"Super Cell" Monocrystalline Solar Cell Characterization from June 12th . .	87
B.6	Battery Charging Test Started at 1:15 p.m. on July 9th	87

Tables

Table

3.1	Operational Entropy Generation Rate for Aircraft Subsystems	24
3.2	Overhead Entropy Generation Rate for Aircraft Subsystems	26
3.3	Total Entropy Generation for Aircraft Subsystems Summed Over the Entire Mission (T_M)	28
3.4	Individual Entropy Generated by a Single Flight	33
3.5	Operational and Overhead Entropy Generation Rate for Energy Harvesting Subsystems	34
3.6	Total Entropy Generation for Energy Harvesting Subsystems Summed Over the Entire Mission (T_M)	34
3.7	Values for Component Buildup Method at 12 m/s	37
4.1	Solar Quality Values	53
4.2	Piezo Systems Inc. Standard Quick-Mount Generator (P/N Q220-A4-103YB) Dimensions and Properties	58

Chapter 1

Introduction

1.1 Motivation

The ability to provide soldiers valuable realtime information from the battlefield can help save lives, both civilian and soldier. Air reconnaissance has helped provide this information in many different ways throughout history, from Zeppelins in World War I hovering over the trenches, sea planes launched from carrier battle groups in World War II searching for the Japanese fleet, the U2 spy plane during the Cold War, satellite imagery, and unmanned air vehicles (UAVs) over the past decade. The idea of UAVs is promising because it takes the airmen out of the skies and can provide longer missions gathering priceless battlefield data. Such UAVs like the Predator and Global Hawk have seen increased action in recent conflicts in Afghanistan and Iraq conducting reconnaissance missions and searching for the enemy. However, these conflicts are becoming more unconventional in the fact that the adversaries are not countries but groups of insurgents and the battles are being conducted in urban environments. With urban warfare becoming more prevalent in recent years, surveillance and reconnaissance is becoming increasingly difficult using traditional methods like the Global Hawk and Predator. One solution to this problem is the use of small UAVs or Micro Air Vehicles (MAVs) to conduct these missions, taking the soldier out of harms way.

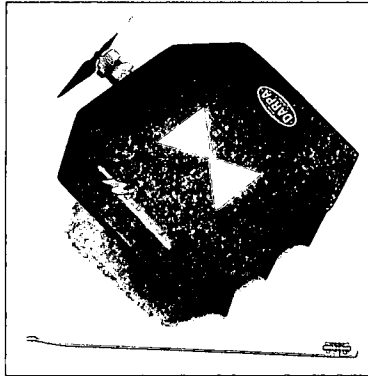


Figure 1.1: AeroVironment Black Widow [1]

1.2 Small Unmanned Air Vehicles

These small aircraft, with wingspans less than 2 meters, have been around for many years on local hobby shop shelves in the form of Radio Controlled (RC) aircraft. The first RC aircraft was designed and flown in 1937 by Walter Good with a wingspan of 6 feet [7]. Since then, RC models have grown even smaller down to wingspans of 9 in. However, RC aircraft are not equipped to perform the missions on the battlefield and the development of the small UAVs or Micro Air Vehicles (MAVs) has received heavy attention in the past decade, especially from the United States Air Force [8]. Having aircraft this size, maneuvering in an urban environment becomes feasible and with the shift in warfare battlefields to these environments, an increased effort in small UAV and MAV development has led to many different aircraft designed for various missions. Aerospace companies like Lockheed Martin and Northrop Grumman have applied their skills in designing large aircraft and invested some effort into designing these smaller aircraft like the Desert Hawk and the Raven in the 1990s, both with wingspans under a 1.5 meters [9]. There has even been aircraft developed that are smaller than the Desert Hawk and Raven, while still capable of performing military missions. AeroVironment, Inc. created a MAV named the Black Widow shown in Figure 1.1. The Black Widow has a wingspan of 6 in and the capability

of providing live color video [1]. Continuing research is ongoing at different Institutes to improve mission capabilities, which will increase the feasibility of utilizing the small UAVs in actual battlefields. One example of this is the Air Force Research Lab effort of flying multiple small UAVs in a coordinated effort to survey a urban environment searching for possible threats. The small UAVs have the ability to investigate targets that were blocked from view at their initial altitude of 500 ft by flying lower to see under the obstruction [10]. However, there are still major obstacles that need to be overcome for these aircraft to play an everyday role in military operations. One such obstacle is the limited flight time constrained by the energy storage options. Due to its size, the Black Widow's maximum flight time is 30 minutes. This is a phenomenal endurance for an aircraft of its size, but limits the type of missions that could be conducted. Larger UAVs exhibit longer flight times but the ability to maintain a presence at a certain location is a critical limitation. Soldiers would need to carry excess batteries or recharging equipment to conduct multiple missions in a finite time period. One solution to extend the mission time could be the use of energy harvesting technology integrated into the aircraft.

1.3 Energy Harvesting

Energy harvesting is associated with taking ambient energy from the environment and turning it into some type of useful energy. It is not a new subject and has been around for centuries. One of the earlier ideas to harvest energy was the windmill, which was first used around the 12th century in Europe to convert wind energy into mechanical energy. Another well known form of energy harvesting is a "hydro power plant." The hydro power plant uses the potential energy of the stored water in the reservoir to turn generators that create electrical energy [11]. Solar and wind farms used in the same manner as the hydro power plant have sprung up across the nation and researchers have worked to improve the

efficiencies and reliability of these systems [3]. Each of these examples demonstrate the ability to harvest energy from the environment but are orders of magnitude larger than anything that could be beneficial to a solution for small UAVs mentioned previously. However, there are many technologies that exist at the scale of the small UAVs or MAVs that may extend mission times. There are solar, thermal, mechanical (vibrations), and wind energies readily available waiting to be harvested and there has been much research conducted to harvest the energy at the micro level. Nishida et al used ambient light and vibrations to provide power to a remote wireless hydrogen sensor [12]. Robbins et al developed a system capable of harvesting wind energy using piezoelectric elements that fluttered in the wind [13]. D.M. Rowe investigated the ability of a thermoelectric device to harvest energy from waste hot water and car engines [14]. Each of these technologies is proven to produce power, but to be a solution to the problem there has to be some benefit to the mission at hand.

1.4 Problem Statement

The idea of using small UAVs and MAVs to conduct intelligence, surveillance, and reconnaissance missions is intriguing. With the latest technology for small UAVs and MAVs, designing the small aircraft to conduct these missions can and has been done. The problem remains the length of time that the aircraft have to conduct the mission because of the limited energy available in batteries. This thesis looks to provide an answer to the problem by investigating the use of solar cell technology and piezoelectric technology incorporated into the aircraft to recharge the batteries of the aircraft when not in flight as shown in Figure 1.2.

With energy harvesting devices, the aircraft is assumed to have the ability stay at a target location for an extended period of time. After either expending all of its energy or

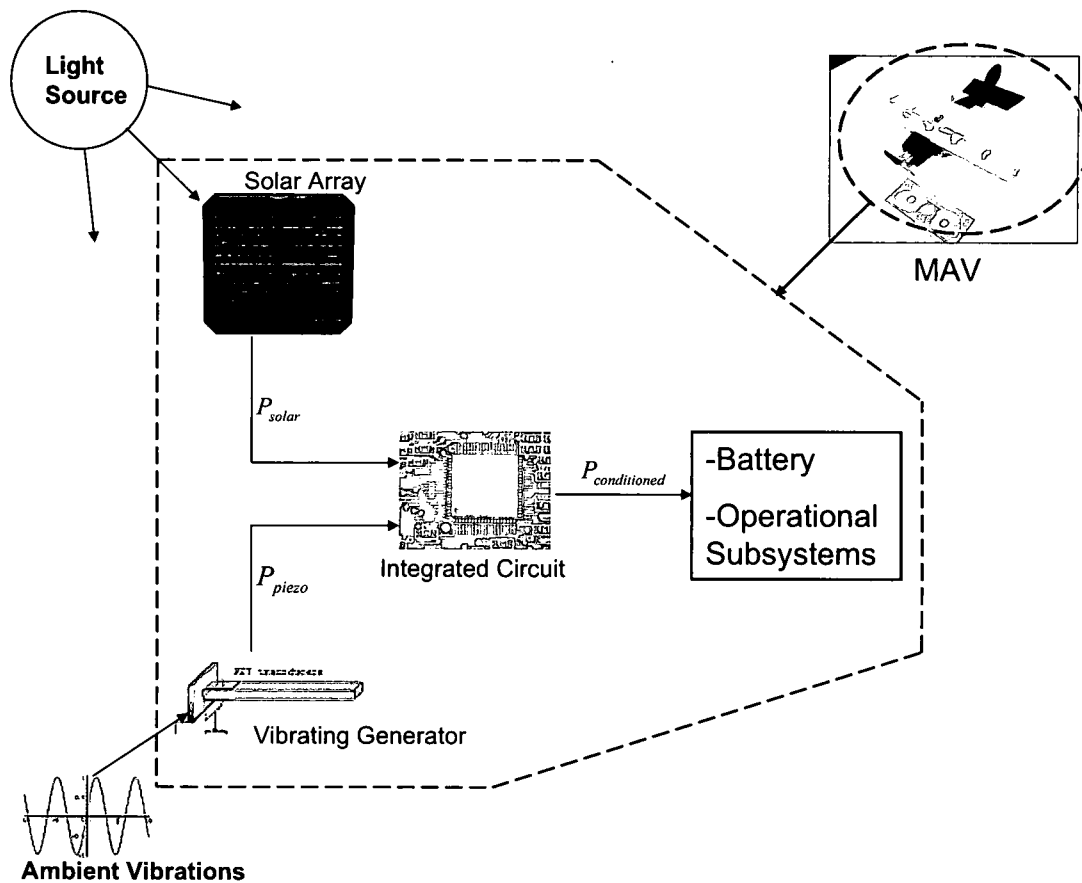


Figure 1.2: Proposed Solution to Small UAV Energy Needs

during a period of downtime in a mission, the small UAV would search for a vibrating energy source or a light source to harvest energy and replenish the energy in its batteries. This thesis will use entropy generation as a metric to analyze the energy harvesting vehicle and also evaluate the potential benefit of integrating solar and piezoelectric energy harvesting devices into the aircraft. The solar cells and piezoelectric devices will be characterized for different energy inputs and then the energy harvesters will be used to recharge a lithium polymer battery. Finally, different solutions will be provided for the integration of the energy harvesters into the aircraft structure.

Chapter 2

Background

This chapter will provide a basic understanding of solar cell and piezoelectric technology and explore the use of the fundamental laws of thermodynamics as an engineering design tool. Additionally, it will look at applications for the three topics and their effect on the research community. Finally, the problem statement and the flow of following chapters in this thesis will be presented.

2.1 Solar Technology

In the United States, solar cell technology has been given a new life in the 21st century with the ever increasing price of oil. Already, the world has taken notice to the shrinking oil supplies and the installation of solar power systems has increase from 300 MW production in 1996 to an estimated 1330 MW in 2002 with Japan leading the world [3]. The push to find an alternative source of renewable energy to replace the use of fossil fuels has helped to increase research in photovoltaic technology. Changing the sun's abundant radiative energy into electricity can supply an application with an abundant energy source. Using solar cells on a small UAV to harvest this energy can provide the aircraft with great potential for new mission opportunities.

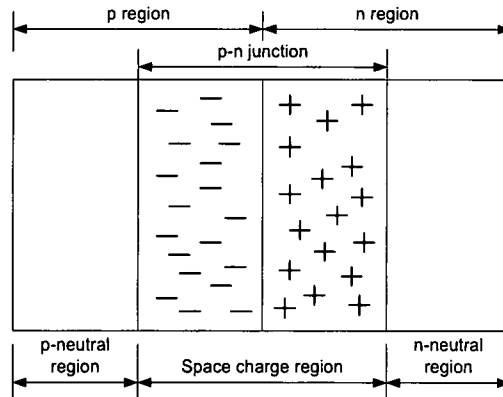


Figure 2.1: The Solar P-N Junction [2]

2.1.1 Basic Principles of Solar Technology

As more applications are being developed with solar cell technology in mind, understanding how they function is vital. The photovoltaic effect, discovered in 1839 by Edmund Bequerel, occurs as a result of light being cast upon two electrodes which creates an electric potential to drive an electrical current through a resistive load [2]. The two electrodes are essentially a p-n junction. The p-n junction in crystalline solar cells are p-doped silicon semiconductors matched to n-doped silicon semiconductor. P-type silicon is doped with boron. Since boron has 3 valence electrons, when bonded to a silicon atom that has 4 valence electrons, a net positive charge is produced by the "hole" created by the missing electron. N-type silicon is doped with phosphorous which has 5 valence electrons and when bonded to silicon, a free electron is produced creating a net negative charge [2, 15]. The p-n junction forms when the two doped regions are brought together and an equilibrium is established at the junction of the two regions, as shown in Figure 2.1. This region of equilibrium separates the positive and negative sides of the silicon creating an electric field [15].

As a result of the electric field, the current flows in one direction. This resembles the

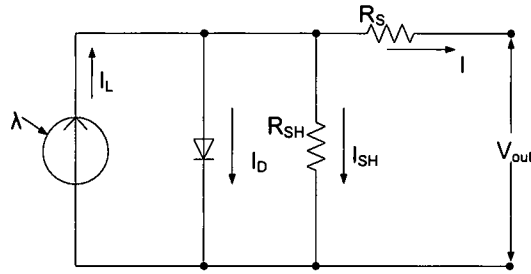


Figure 2.2: Equivalent Circuit of a Solar Cell [3]

property of the diode and can be modeled as shown in Figure 2.2. The solar cell generates current (I_L) and experiences losses from its diode characteristics (I_d) and shunt-leakages (I_{sh}) [3].

$$I_{total} = I_L - I_d - I_{sh} \quad (2.1)$$

When a solar cell is cast under a light, the energy from the light causes electrons to flow free and travel across the p-n junction. The packets of energy in light are photons and their energy relies on the frequency of the light. The photons related to the visible section of the light spectrum contain enough energy to excite electrons to higher energy levels in solids, thus allowing the electrons to move freely [4]. Figure 2.3 illustrates the light hitting the solar cell and exciting the electron that in turn creates a current to flow through the load.

2.1.2 Solar Cell Applications

Solar cells come in a variety of sizes, materials, and configurations suitable for many different applications. Three common types of solar cells are monocrystalline, polycrystalline, and amorphous silicon solar cells. Of these three types of solar cells, monocrystalline cells are the most efficient, roughly 14-18%, followed by polycrystalline cells at around 10-12%, and finally amorphous solar cells with about 5% conversion efficiency.

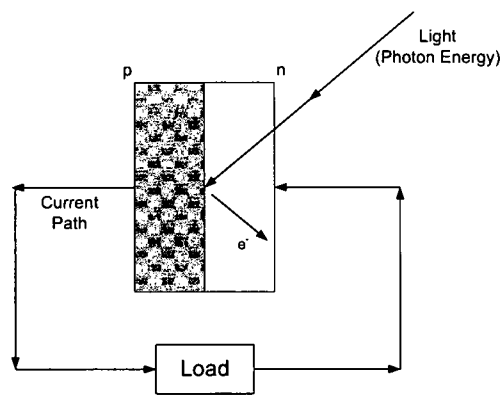


Figure 2.3: A Solar Cell Being Struck by Light [4]

However, with the higher efficiency comes a higher price due mainly to manufacturing costs. The advantage of polycrystalline cells in manufacturing is that they are not affected by imperfections with the cell that would affect monocrystalline cells and amorphous cells use 1% of the material needed for monocrystalline cells. Amorphous cells also have the advantage of being highly flexible. Other new technologies, thin-film, spherical, organic, and multijunction cells to name a few, have been developed to increase efficiencies and lower manufacturing costs. Thin film technology has shown efficiencies of 18% in laboratory settings while keeping manufacturing costs down. Multijunction cells, which utilize more than one p-n junction to capture multiple energy levels of light to improve efficiency, have shown efficiencies as high as 40% with the assistance of concentrated light [3, 2, 4, 16].

Research to increase the efficiency and lower manufacturing cost has increased the use of solar cells in the world. Nelson acknowledged this by stating, "Photovoltaics first became competitive in contexts where conventional electricity supply is most expensive, for instance, for remote low power applications such as navigation, telecommunications, and rural electrification and for enhancement of supply in grid-connected loads and peak use" [4]. Whether it be grid connected systems or stand alone systems, the potential for solar cell applications is great. Grid connected systems are becoming more popular as years pass. Countries are providing incentives to customers who install solar cells on their land. These solar cells can be used to power the owner's grid or to sell back to electric companies. Japan developed a program with the hopes of installing photovoltaic power systems on 70,000 roofs [2]. These are examples of large scale systems integration that have led to the opportunities for small scale integration of solar harvesting as a solution to engineering problems. This is demonstrated by the use of solar cells implemented into automobiles and even onto a camel where doctors in Africa use a photovoltaic powered refrigeration system strapped to a camel's back to keep medical supplies cold seen in Figure 2.4 [3]. On an even smaller scale, Nishida et al developed a wireless hydrogen



Figure 2.4: Camel Carrying Refrigeration Unit [3]

sensor the uses ambient light and vibrations for power [12]. The sensor can be placed at a remote location to help sense hydrogen concentration and uses crystalline solar cells as part of the power supply.

The use of solar energy harvesting for the camel refrigeration unit and the wireless hydrogen sensor, provided innovative solutions to problems that were difficult to solve without it. This is evident in the solution of continuous electrical flight demonstrated by an aerospace company located in San Diego, AC Propulsion. AC Propulsion designed an aircraft, designated SoLong, capable of flying for 48 continuous hours on harvested solar power alone. SoLong has a wingspan of 15.6 ft and weighs roughly 28 lbs. with the solar panels integrated into the wing. The aircraft used a combination of soaring, to conserve battery power, and motor powered flight to stay aloft [17]. NASA is also interested in solar sustained flight and contracted out the construction of Helios to AeroVironment. Helios was to fly only on solar electrical power alone during the day like SoLong but at much higher altitudes with the goal of sustaining 24 hours of flight time with the aid of fuel cells for energy at night. Helios is much larger than SoLong with a wingspan of 247 ft and an empty weight of 1332 lbs [18]. Although these two aircraft are much larger than the proposed aircraft in this thesis, they demonstrate the ability and potential of solar energy harvesting at the MAV level.

2.2 Piezoelectric Technology

Another type of energy harvesting chosen for this study was vibrational energy harvesting utilizing piezoelectric materials. There are many sources of mechanical vibrations in urban environments that could provide a small UAV with extra power to supplement battery power. Taking advantage of the special properties of piezoelectric materials can increase the abilities of a small UAV and provide the application with more potential for success.

2.2.1 Basic Principles of Piezoelectric Technology

Since the 1880s, scientists have been studying a phenomenon called piezoelectricity. It occurs in certain materials that exhibit special properties when induced to a strain or electrical potential. These special properties are known as the direct and converse piezoelectric effect. The direct effect takes place as a result of a mechanical load being applied to the piezoelectric material. This load induces a strain, and in the elastic region of the stress-strain curve, the piezoelectric material creates an electric potential between two electrodes. The converse effect works in the reverse direction. When an electric potential is placed across two electrodes on the piezoelectric material, a mechanical response is produced in the material [19, 5]. The polarity of the base structure of the crystalline piezoelectric material provides the material with one of its main properties. Within the crystal are unit cell structures that contain a polar axis that separate positive and negative charges. The positive and negative charges separated by a fixed distance are known as electric dipoles and provide the piezoelectric material with the ability to produce the direct and converse effect. In association with the direct effect, when the material is strained the dipoles experience a rotation that results in a current that can flow through the electrodes. Conversely, applying an electric field to the piezoelectric material results in a charge attrac-

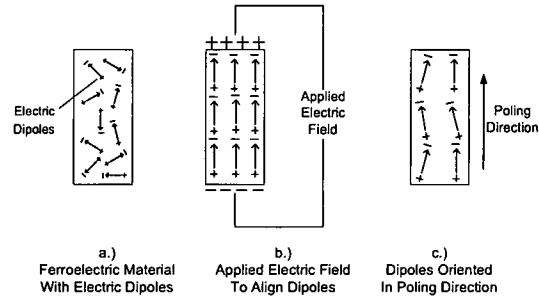


Figure 2.5: Poling Process for Synthetic Piezoelectric Materials [5]

tion between dipoles. The attraction of opposite charges creates a rotation in the dipoles that produces a strain in the material [5].

There are many natural materials that demonstrate the piezoelectric effect. However, this effect is small. In the mid 1900s, piezoelectric materials with better properties were developed which increased the potential of the piezoelectric materials for different applications. These synthetic piezoelectric material are made by adding Lead (Pb), Zirconium (Zr), and Titanium (Ti) to basic piezoelectric materials. This combination forms the common piezoelectric PZT, Lead-Zirconium-Titanate. There other common synthetic piezoelectric materials known as Barium Titanate and Sodium-potassium niobates [5]. With synthetic piezoelectric materials, the electric dipoles are oriented randomly resulting in weak piezoelectric properties that need to be aligned properly. To do this, the material is heated above the Curie Temperature and a strong electric field is placed across the electrodes lining the dipoles in the proper direction. This process is illustrated in if Figure 2.5.

2.2.2 Piezoelectric Applications

Using a piezoelectric bimorph beam as a power generator has been a widely researched subject in the academic world [20, 21, 22, 23, 24, 12, 25, 26, 27]. In particular, Sodano et al. demonstrated the ability of piezoelectric energy harvesters in the form of

cantilever beams to charge nickel metal hydride batteries [23]. Two types of piezoelectric materials were used in the experiment, PZT and Macro Fiber Composites (MFC). Sodano et al. showed that a 2.5 x 2.375 in. PZT plate was capable of charging a 300 mAh battery to 90% full charge in 6 hours vibrating the beam at resonance. Roundy and Wright developed two micro-beam generators constrained in size to 1 cm² with the ability to produce 375 μ W of power at a 120 Hz [20]. The beams were then used to power a custom 1.9 GHz radio transmitter from the energy harvested from the 120 Hz vibration source. Looking at a obscure vibration source, Lal et al. developed a piezoelectric micro-generator powered by particles emitted from radioisotopes [27]. The kinetic energy from these particles is used to provide the mechanical energy in a unimorph piezoelectric beam. Using the particles as an energy source allows the generators to smaller than 1 mm³.

Along with the research for better vibrational energy harvesters, work has been done to increase the output of the harvesters with better circuit designs and tunable beams [28, 29, 30, 31, 32, 33, 34]. Badel et al. used a synchronized switch technique in conjunction with a cantilever beam that resulted in a 400% increase in power output [28]. In an attempt to change the natural frequency of the cantilever beam, Charnegie et al. developed a method a tuning the stiffness of the beam with a piezoelectric layer and a shunt circuit [32]. The shunt circuit was varied resulting in an altered stiffness and natural frequency. Using this technique allows the natural frequency of the beam to be matched to the source vibrations thus increasing the power output of the beam. Tunable beams coupled with optimized harvesting circuit designs can provide applications with a promising future.

2.3 Thermodynamic Analysis

An approach for the analysis of engineering systems has been gaining interest in the aerospace world. This approach is centered around thermodynamics and involves either

entropy generation or exergy destruction. Entropy is the a measure of disorder in a system and always increasing while exergy can be defined as the potential to do work. Using entropy generation and exergy destruction in the analysis of aerospace systems provides a single metric to evaluate possible designs of various aircraft subsystems. This process provides information on energy demands of the subsystems and the effects they might have on other subsystems.

Many different studies have used the thermodynamic approach to study different aircraft systems [35, 36, 37, 38, 39, 40, 41, 42]. Specifically, Hallinan et al. chose the technique of entropy generation minimization (EGM) to analyze an aircraft fitted with a radar array [35]. Their study took an indepth look at the addition of thermoelectric (TE) devices integrated between the radar array and the cooling system. The TE devices converted the heat rejected from the radar array into electrical energy which was fed back into the energy provided to the array. Using EGM, they showed that theoretically the TE devices were beneficial to the overall aircraft design. This approach is the basis for the entropy analysis section that will be presented later in this thesis. Ahlers et al. used EGM to study a multifunctional aircraft skin [41]. The EGM process was used to help design the skin layer of the aircraft and optimize the thickness and type of skin. Finally, Butt studied the effects of morphing in fighter aircraft using exergy analysis [42]. His study demonstrated that morphing during a mission decreases the exergy destruction, thus reducing the fuel consumed during a mission.

2.4 Chapter Summary

Solar and mechanical energy harvesting was analyzed. Design applications for each of the energy harvesting techniques were presented. The use of energy harvesting appears to be a solution for a small UAV to maintain a persistent presence at any location.

Additionally, the use of the laws of thermodynamics as an engineering design tool was researched and multiple examples were presented. The remaining chapters of the thesis will provide a detailed study of the use of energy harvesting for a small UAV. The following chapter will present an entropy analysis of the small UAV and the effects of energy harvesting to the aircraft and during a generic mission. Chapters 4 and 5 will discuss the two energy harvesting techniques, solar and mechanical chosen for this application. The first of the two chapters will provide characterizations of the energy harvesting techniques to assist in the analysis in Chapter 5. Chapter 5 will then provide integration ideas for the energy harvesting devices. These remaining chapters will provide a better understanding of the benefits of energy harvesting for small UAVs and how solar and piezoelectric devices can be added to aid the performances of the aircraft.

Chapter 3

Entropy Generation Analysis

This chapter will provide an analysis of the small UAV using entropy generation as a metric to evaluate system and subsystem performance during a notional mission. It will explain the steps needed to calculate entropy generation and examine the entropy generated by the small UAV during steady level flight. From there, this chapter will present a mission simulation to compare the small UAV with and without energy harvesting and provide an aerodynamic analysis that will be used in the mission simulation.

3.1 Entropy Generation

The performance of engineering devices can be determined using entropy generation as a criteria for comparison [43]. Just as Hallinan et al. used entropy generation as a metric to analyze thermoelectric energy harvesting on a radar aircraft, it is used to study the small UAV's for this research [35]. The approach presented in the following sections is similar to the approach taken by Hallinan et al. However, due to the major differences in aircraft size and complexity, changes were made in certain calculations and system definitions. For example, Hallinan et al. were limited in their control volume selection because of the vast number of aircraft subsystems and interactions among these subsystems that may not have any affect on the subsystem of interest [35]. On the other hand, the RC aircraft chosen for this study has fewer subsystems, each affecting the entire system. With this in

mind, the following sections will present the calculations of entropy generation define the control volume for the small UAV of this research.

3.1.1 Calculating Entropy Generation

The total entropy generated was calculated using equation 3.1.

$$S_{gen,Total} = S_{gen,operational,Total} + S_{gen,overhead,Total} \quad (3.1)$$

where S_{gen} is entropy generation and the subscripts operational and overhead represent the corresponding entropies. The operational entropy generated is due to the inefficiencies of the subsystems and the overhead entropy generated is associated with the masses of the subsystems in the aircraft. Each term, operational and overhead, is calculated over a specified time for each of the subsystems shown in the control volume and summed together, as seen in equation 3.2,

$$S_{gen,Total} = \sum_{i=1}^N S_{gen,operational,i} + \sum_{i=1}^N S_{gen,overhead,i} \quad (3.2)$$

where $i=1,...,N$ are each of the subsystems of the aircraft. To determine the total entropy of the system and subsystems, a control volume needed to be selected. The next section discuss the selection of the control volume.

3.1.2 Control Volume Selection

The airplane used in this study is a Radical RC Micro Stick electric flyer seen in Figure 3.1. This aircraft was chosen because of it size and the fact that it is capable of a 15 minute flight time. The control volume chosen for the Micro Stick surrounds the entire vehicle. Each system in the aircraft, the motor, servo, etc., is "connected" to some degree, as each subsystem affects the others. The entire system inside the control volume

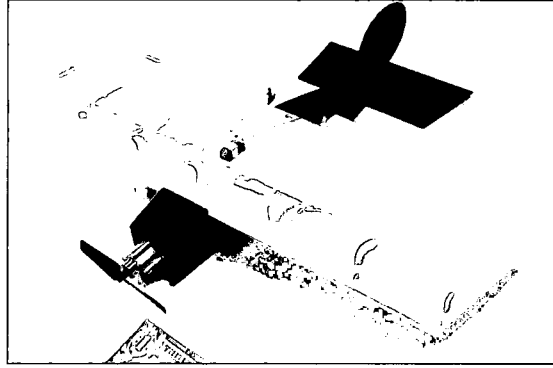


Figure 3.1: RC Aircraft Used in Analysis

is shown in Figure 3.2. The corresponding power connections are shown with the dotted arrows. As a consequence of inefficiencies of each subsystem, there is an associated heat loss to the environment, pictured as the solid arrows in the figure. These heat losses should be noted because they are important to the calculation of the operational entropy generated by the aircraft. The operational entropy will be discussed in the following section.

3.1.2.1 Operational Entropy Generation

Calculating the operational entropy generation first requires the determination of the power into and heat produced for each of the components. To demonstrate this calculation, the electric motor operational entropy is presented. As shown in Figure 3.3, the motor needs an input power (\dot{W}_{in}) to operate, calculated by multiplying the input current (I) by the voltage (V). Part of the input power is converted to a power supplied to the propeller (\dot{W}_{out}) and due to the inefficiency of the motor, the rest is heat (\dot{Q}) rejected to the environment. The heat rate rejected by the motor divided by the ambient environment temperature is the operational entropy rate for the motor calculated in equation 3.3.

$$\dot{S}_{gen,operational,motor} = \frac{\dot{Q}}{T_0} = \frac{\dot{W}_{in}(1 - \eta_{motor})}{T_0} \quad (3.3)$$

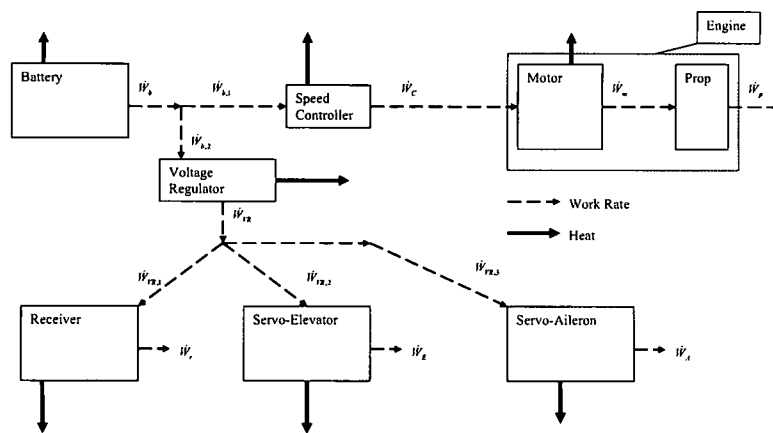


Figure 3.2: Control Volume for Micro Stick Aircraft

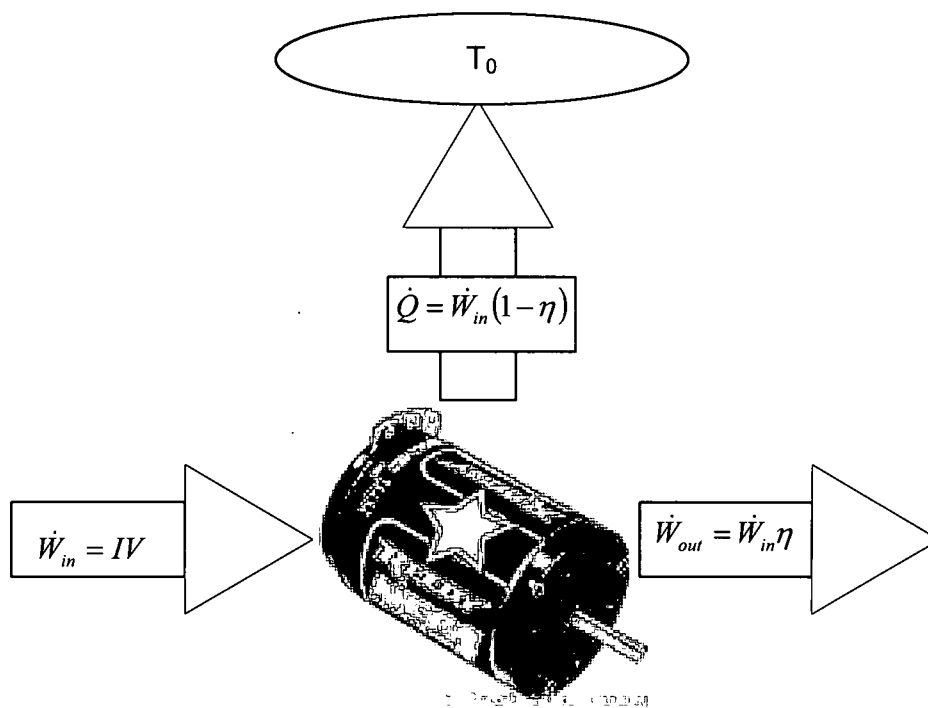


Figure 3.3: Illustration of Operational Entropy

where η_{motor} is the efficiency of the motor, and T_0 is the ambient environment temperature in Kelvin (K). This process is repeated for each component and the results are summarized in Table 3.1. Appendix A details the complete operational entropy calculations for the subsystems. To simplify the entries, the term β was introduced as the ratio of input power to output power at electrical nodes where the current splits into two directions. Recalling Figure 3.2 and applying Kirchhoff's current law that states that the current into a node is equal to the current coming out and the following results

$$\dot{W}_b = \dot{W}_{b,1} + \dot{W}_{b,2} \quad (3.4)$$

Dividing equation 3.4 by \dot{W}_b , it becomes

$$1 = \frac{\dot{W}_{b,1}}{\dot{W}_b} + \frac{\dot{W}_{b,2}}{\dot{W}_b} \quad (3.5)$$

Denoting

$$\beta = \frac{\dot{W}_{b,1}}{\dot{W}_b} \quad (3.6)$$

and also calling

$$\beta_i = \frac{\dot{W}_{VR,i}}{\dot{W}_{VR}} \quad (3.7)$$

where $i=1, 2$, and 3 , the derivation of the β term is completed [44]. The next section will discuss the calculation of overhead entropy generation.

3.1.2.2 Overhead Entropy Generation

The overhead entropy generation corresponds to the components presented in the previous section on operational entropy. The overhead entropy generation for this aircraft was calculated using equation 3.8.

Table 3.1: Operational Entropy Generation Rate for Aircraft Subsystems

Aircraft Subsystem	Operational $\dot{S}_{gen}/\dot{W}_{battery}$
Battery	$\frac{(1-\eta_{battery})}{\eta_{battery} T_0}$
Speed Controller	$\frac{\beta(1-\eta_{controller})}{T_0}$
Motor	$\frac{\beta\eta_{controller}(1-\eta_{motor})}{T_0}$
Voltage Regulator	$\frac{(1-\beta)(1-\eta_{regulator})}{T_0}$
Receiver	$\frac{(1-\beta)\beta_1\eta_{regulator}(1-\eta_{receiver})}{T_0}$
Aileron	$\frac{(1-\beta)\beta_2\eta_{regulator}(1-\eta_{aileron})}{T_0}$
Elevator	$\frac{(1-\beta)\beta_3\eta_{regulator}(1-\eta_{elevator})}{T_0}$

$$\dot{S}_{\text{gen,overhead},i} = m_i \left(1 + \frac{m_{\text{non-operational systems}}}{m_i} \right) \dot{G} \quad (3.8)$$

where $\dot{S}_{\text{gen,overhead},i}$ is the overhead entropy generated by a subsystem, m_i is the mass of the subsystem, $m_{\text{non-operational systems}}$ is the mass of the non-operational systems needed to support the operational subsystems, and \dot{G} is the overhead entropy generation per mass per time [35]. The term $1 + m_{\text{non-operational systems}}/m_i$ is a correction factor to a given subsystem mass which accounts for the amplifying effect of changes in this mass on non-operational systems, i.e. the structure, skin, etc., needed to support the mass of the operational subsystem over the entire mission. In this analysis two figures of merit are used. The first, m_i/\dot{W}_i , is used to compare the operational component's masses to their corresponding work rates as a mass per power ratio. The second figure of merit is $m_{\text{non-operational systems}}/m_i$. \dot{G} is a way of determining the work produced by the engine and associated entropy generated to increase the potential and kinetic energy of the aircraft while overcoming the induced drag force during the specified time frame. \dot{G} is expressed as

$$\dot{G} = \frac{\left[\frac{d}{dt} \left(\frac{1}{2} V^2 \right) + \frac{d}{dt} (g(z) dz) + \frac{C_L}{\pi A R e} g[z(x)] \frac{dx}{dt} \right] (1 - \eta_{\text{motor}})}{\eta_{\text{engine}} T_0} \quad (3.9)$$

where V is aircraft velocity, g is a the gravity constant, z is the altitude, C_L is the lift coefficient, AR is the aspect ratio, e is the span efficiency, and η_{engine} is the efficiency of the motor and propeller combined. The overhead entropy generation rates for the subsystems are listed in Table 3.2. The remaining subsystem's overhead entropy generated is presented in Appendix A.

3.1.2.3 Total Entropy Generation

To determine the total entropy generation of the aircraft, first, the operational entropy rates for each subsystem were multiplied by the flight time, T_M . The overhead entropy rates are affected in the same manner. \dot{G} thus becomes

Table 3.2: Overhead Entropy Generation Rate for Aircraft Subsystems

Aircraft Subsystem	Overhead $\dot{S}_{\text{gen}}/\dot{W}_{\text{battery}}$
Battery	$\left[\frac{m_{\text{battery}}}{\dot{W}_{\text{battery}}} \right] \dot{G} \left[1 + \frac{m_{\text{non-op-subsystems}}}{m_{\text{battery}}} \right]$
Speed Controller	$\left[\frac{m_{\text{controller}}}{\dot{W}_{\text{controller}}} \right] (\beta \eta_{\text{controller}}) \dot{G} \left[1 + \frac{m_{\text{non-op-subsystems}}}{m_{\text{controller}}} \right]$
Motor	$\left[\frac{m_{\text{motor}}}{\dot{W}_{\text{motor}}} \right] (\beta \eta_{\text{controller}} \eta_{\text{motor}}) \dot{G} \left[1 + \frac{m_{\text{non-op-subsystems}}}{m_{\text{motor}}} \right]$
Voltage Regulator	$\left[\frac{m_{\text{regulator}}}{\dot{W}_{\text{regulator}}} \right] ((1 - \beta) \eta_{\text{regulator}}) \dot{G} \left[1 + \frac{m_{\text{non-op-subsystems}}}{m_{\text{regulator}}} \right]$
Receiver	$\left[\frac{m_{\text{receiver}}}{\dot{W}_{\text{receiver}}} \right] ((1 - \beta) \beta_1 \eta_{\text{receiver}}) \dot{G} \left[1 + \frac{m_{\text{non-op-subsystems}}}{m_{\text{receiver}}} \right]$
Aileron	$\left[\frac{m_{\text{aileron}}}{\dot{W}_{\text{aileron}}} \right] ((1 - \beta) \beta_2 \eta_{\text{aileron}}) \dot{G} \left[1 + \frac{m_{\text{non-op-subsystems}}}{m_{\text{aileron}}} \right]$
Elevator	$\left[\frac{m_{\text{elevator}}}{\dot{W}_{\text{elevator}}} \right] ((1 - \beta) \beta_3 \eta_{\text{elevator}}) \dot{G} \left[1 + \frac{m_{\text{non-op-subsystems}}}{m_{\text{elevator}}} \right]$

$$G = \frac{[(\frac{1}{2}V^2) + (gz_{alt}) + \frac{C_L}{\pi A R e} g V T_M] (1 - \eta_{motor})}{\eta_{engine} T_0} \quad (3.10)$$

Recalling equations 3.1 and 3.2, adding the operational and overhead entropies of each subsystem together for the entire flight gives the total entropy generation for the subsystems. These are summarized in Table 3.3.

3.1.2.4 Entropy Generated During Flight

Determining the efficiency sensitivity of each component during a single flight was the initial intent of the analysis. The purpose of this study was to determine what subsystem's efficiencies affected the overall system the most. For the analysis, the mission time was set to 10 min for the study. Steady level flight at a cruise velocity of 9 m/s was used to determine the corresponding C_L of 0.449. The current for the motor was assumed to be 4.5 amps while the current for the regulator was .022 amps. These values came from flight tests that lasted 10 minutes. Knowing that a 740 mAh can supply 740 mA for 1 hour, a battery that drains in 10 minutes supplied roughly 4.5 amps to the motor. The reason for the small regulator current is because of the assumption that the servos are used minimally during the flight and the receiver has a small current draw. An analysis was conducted by varying the efficiencies two at a time for the four components in series: the battery, controller, the motor, and the propeller. The following results will be for a varying battery efficiency coupled to each of the other efficiencies.

The first comparison is between the battery and controller. Figure 3.4 is a 3-D graph with battery efficiency and controller efficiency on the x-axis and y-axis and the total S_{gen} on the z-axis. The graph shows that neither the battery nor the controller affects the system more than the other and illustrates that the entropy generation decreases at the same rate for both the battery and controller as the efficiencies increase. The next figure, Figure 3.5, is of the battery and motor efficiencies with the graph set up the same as Figure

Table 3.3: Total Entropy Generation for Aircraft Subsystems Summed Over the Entire Mission (T_M)

Aircraft Subsystem	Total S_{gen}/\dot{W}_b
Battery	$\frac{(1-\eta_b)T_M}{\eta_b T_0} + \left[\frac{m_b}{\dot{W}_b} \right] G \left[1 + \frac{m_{non-op-subsystems}}{m_b} \right]$
Speed Controller	$\frac{\beta(1-\eta_c)T_M}{T_0} + \left[\frac{m_c}{\dot{W}_c} \right] (\beta\eta_c)G \left[1 + \frac{m_{non-op-subsystems}}{m_c} \right]$
Motor	$\frac{\beta\eta_c(1-\eta_m)T_M}{T_0} + \left[\frac{m_m}{\dot{W}_m} \right] (\beta\eta_c\eta_m)G \left[1 + \frac{m_{non-op-subsystems}}{m_m} \right]$
Voltage Regulator	$\frac{(1-\beta)(1-\eta_{vr})T_M}{T_0} + \left[\frac{m_{vr}}{\dot{W}_{vr}} \right] ((1-\beta)\eta_{vr})G \left[1 + \frac{m_{non-op-subsystems}}{m_{vr}} \right]$
Receiver	$\frac{(1-\beta)\beta_1\eta_{vr}(1-\eta_r)T_M}{T_0} + \left[\frac{m_r}{\dot{W}_r} \right] ((1-\beta)\beta_1\eta_r)G \left[1 + \frac{m_{non-op-subsystems}}{m_r} \right]$
Aileron	$\frac{(1-\beta)\beta_2\eta_{vr}(1-\eta_a)T_M}{T_0} + \left[\frac{m_a}{\dot{W}_a} \right] ((1-\beta)\beta_2\eta_a)G \left[1 + \frac{m_{non-op-subsystems}}{m_a} \right]$
Elevator	$\frac{(1-\beta)\beta_3\eta_{vr}(1-\eta_e)T_M}{T_0} + \left[\frac{m_e}{\dot{W}_e} \right] ((1-\beta)\beta_3\eta_e)G \left[1 + \frac{m_{non-op-subsystems}}{m_e} \right]$

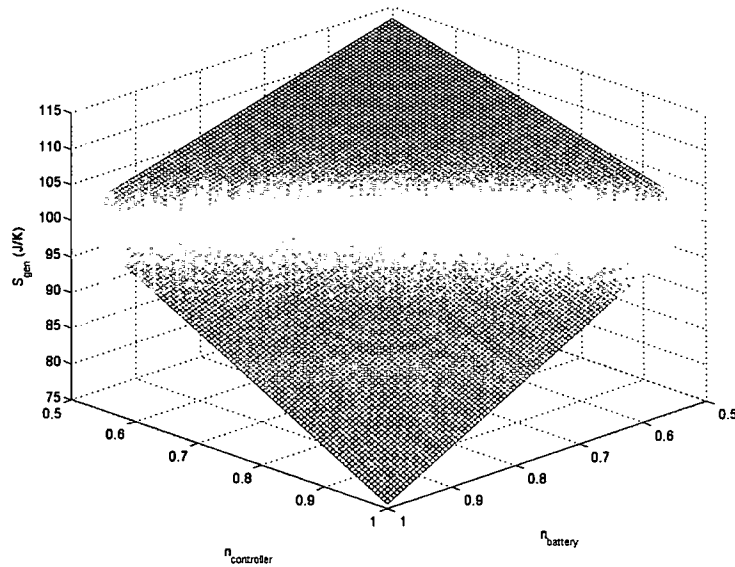


Figure 3.4: Total Entropy Generated vs. Battery Efficiency and Controller Efficiency

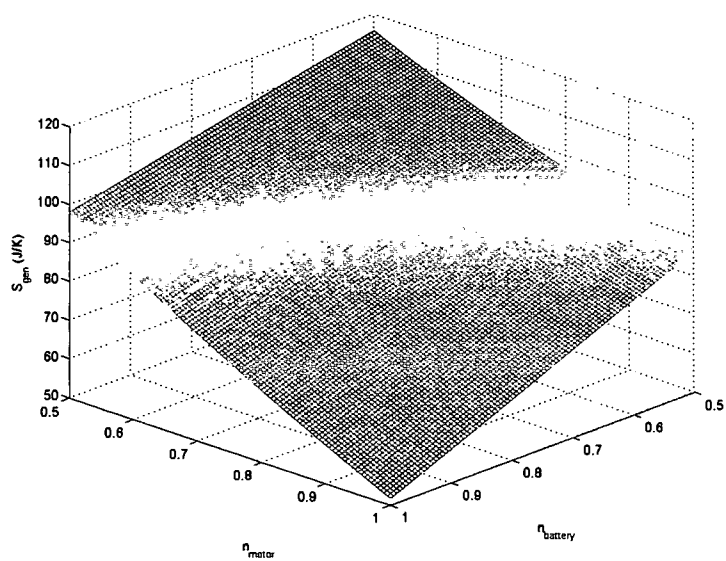


Figure 3.5: Total Entropy Generated vs. Battery Efficiency and Motor Efficiency

3.4. Figure 3.5 shows that the entropy generated is more sensitive to the motor than the battery efficiency. Similarly, Figure 3.6 demonstrates the total entropy generated is more sensitive to the propeller efficiency much like the motor. Since the entropy generation is equally sensitive to the battery efficiency and the controller efficiency, and the motor and propeller efficiencies have more effect on entropy generation than the battery, the motor and propeller efficiencies were compared in Figure 3.7. The results show that the entropy generated is equally sensitive to the motor efficiency as the propeller efficiency. Overall, this analysis showed that modifying motor or propeller efficiencies will have the greatest effect on the total entropy generated relative to the other subsystems. To further this study, the total entropy over the entire flight for the given efficiencies will be analysis next.

The purpose of the next analysis was to calculate the entropy generated by the individual components during the flight to determine the order of magnitude of the component's entropy generation. For the inputs presented for the sensitivity analysis, the entropy generated by the UAV were calculated following the steps detailed in the previous sections. The total entropy generated for a single flight was 82.1 J/K. The individual entropies for the components are summarized in Table 3.4. A closer look at the table reveals that the motor and propeller dominate the operational entropy generated. This is due to the fact that the efficiencies of these two devices are much lower than the rest of the subsystems. The propeller was estimated to be about 60% efficient while the electric motor is roughly 70% efficient at normal operating conditions. As is evident in the overhead entropy generation column, each component produces roughly the same overhead entropy except for the battery. This is due to the fact that the battery is much more massive than the other components and therefore needs more energy to support it in flight. Among the operational and overhead entropy generated, the operational entropy dominates generating roughly 88% of the total entropy generation and, again, is due mainly to the inefficiencies of the motor and propeller. Increasing the efficiency of either would result in more energy being supplied to

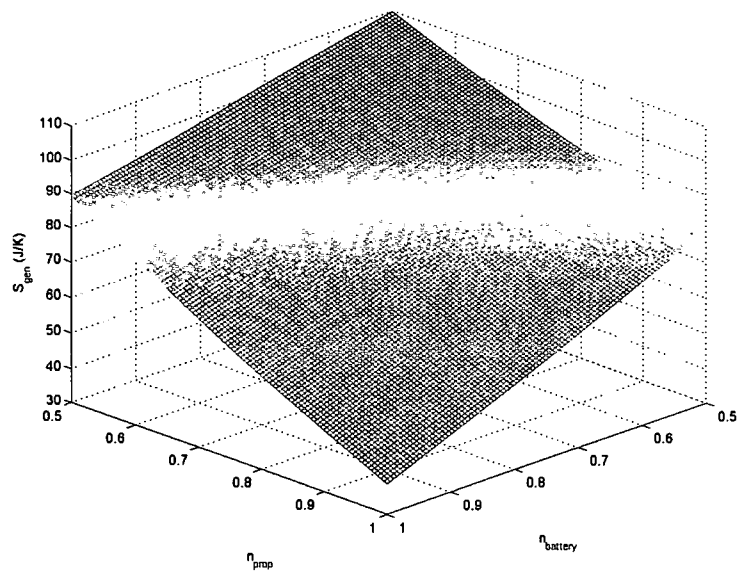


Figure 3.6: Total Entropy Generated vs. Battery Efficiency and Propeller Efficiency

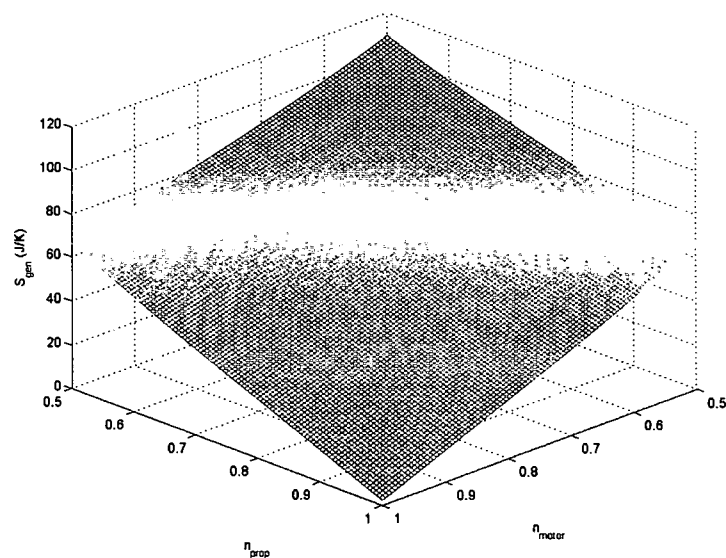


Figure 3.7: Total Entropy Generated vs. Motor Efficiency and Propeller Efficiency

conduct the flight and produce longer flight times. The next section will take this analysis a step further and introduce a generic mission in which to compare added energy harvesting to the small UAV and its effects over a sustained period of time.

3.2 Mission Simulation

The next part of the analysis examines the energy harvesting small UAV using a mission simulation designed in order to compare it to the same UAV without energy harvesting. The control volume for the energy harvesting UAV is given in Figure 3.8 and the entropy calculations for the additional devices are given in Tables 3.5 and 3.6. Appendix A provides detailed look at the energy harvesting's entropy generation. Referring back to original control volume of the Microstick airplane, Figure 3.2, the difference between the two aircraft is the addition of solar panels, piezoelectric devices and a recharging circuit. For this analysis, it was decided that the piezoelectric devices would be used to supply power to a sensor and not used to charge the battery. Therefore, the piezoelectric device would only be counted as a non-operational system in the mission simulation. The remainder of this chapter will present the mission simulation and its results. From this point, the small UAV without energy harvesting will be called the Base Aircraft and the energy harvesting small UAV will be called the EH Aircraft.

3.2.1 Mission Definition

The mission was designed to maximize the total amount of reconnaissance flight time at a certain target location while minimizing battery recharging time necessary to carry out this mission. Figure 3.9 provides an illustration of the Base Aircraft's mission. For the Base Aircraft, the mission was split into four sections, a dash to the target, loitering and observing at the target, a dash back to its starting location, and a recharging segment.

Table 3.4: Individual Entropy Generated by a Single Flight

Components	Operational (J/K)	Overhead (J/K)
Battery	5.83	2.07
Controller	5.52	1.04
Motor	31.44	1.41
Propeller	29.34	1.09
Regulator	0.03	1.01
Receiver	0.02	1.19
Aileron	0	1.06
Elevator	0	1.06

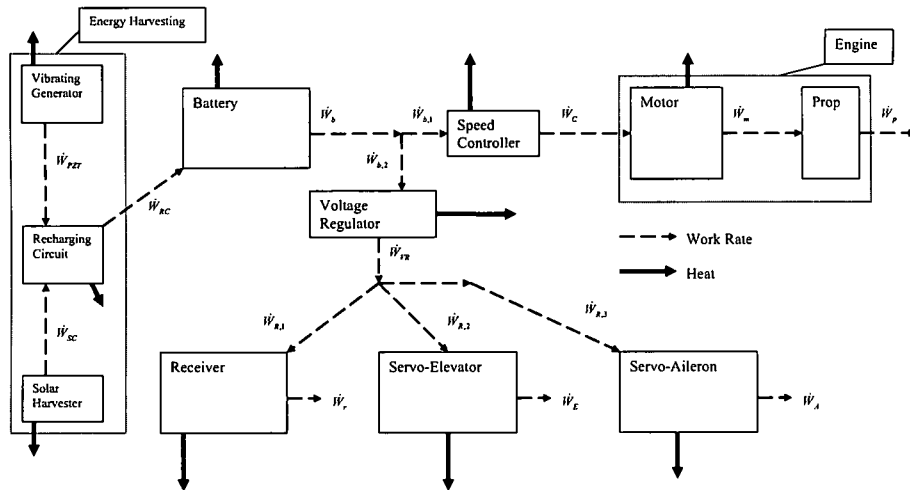


Figure 3.8: Control Volume for EH Aircraft

Table 3.5: Operational and Overhead Entropy Generation Rate for Energy Harvesting Subsystems

Aircraft Subsystem	Operational S_{gen}/\dot{W}_b	Overhead S_{gen}/\dot{W}_b
Recharging Circuit	$\frac{\dot{W}_{solar}(1-\eta_{circuit})}{T_0 \dot{W}_{battery}}$	$\left[\frac{m_{circuit}}{\dot{W}_{circuit}} \right] \left(\frac{\dot{W}_{circuit}}{\dot{W}_{battery}} \right) \dot{G} \left[1 + \frac{m_{non-op-subsystems}}{m_{circuit}} \right]$
Solar Cell	$\frac{P_{solar}(1-\eta_{solar})}{T_0 \dot{W}_{battery}}$	$\left[\frac{m_{solar}}{\dot{W}_{solar}} \right] \left(\frac{\dot{W}_{solar}}{\dot{W}_{battery}} \right) \dot{G} \left[1 + \frac{m_{non-op-subsystems}}{m_{solar}} \right]$

Table 3.6: Total Entropy Generation for Energy Harvesting Subsystems Summed Over the Entire Mission (T_M)

Aircraft Subsystem	Total S_{gen}/\dot{W}_b
Recharging Circuit	$\frac{\dot{W}_{sc}(1-\eta_{rc})T_M}{\dot{W}_b T_0} + \left[\frac{m_{rc}}{\dot{W}_{rc}} \right] \left(\frac{\dot{W}_{rc}}{\dot{W}_b} \right) G \left[1 + \frac{m_{non-op-subsystems}}{m_{rc}} \right]$
Solar Cell	$\frac{P_{sc}(1-\eta_{sc})T_M}{\dot{W}_b T_0} + \left[\frac{m_{sc}}{\dot{W}_{sc}} \right] \left(\frac{\dot{W}_{sc}}{\dot{W}_b} \right) G \left[1 + \frac{m_{non-op-subsystems}}{m_{sc}} \right]$

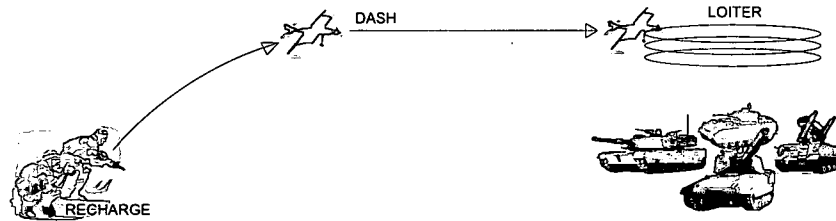


Figure 3.9: Base Aircraft Mission Illustration

After each recharging section, the Base Aircraft repeats these steps for a defined time period referred to as a "day."

Figure 3.10 provides an illustration of the EH Aircraft's mission. The EH Aircraft mission involves a dash to the target, loitering and observing until the battery charge is too low, perching and recharging at the target location until the "day" ends and then a dash back to the starting location. It should be noted that the EH Aircraft only harvests and uses the energy during the recharging stage, and not during flight to supplement the power drawn from the battery, where it has either perched or landed somewhere at the target location. It should also be noted that the issue of perching is not researched for this thesis. The difference between the two missions is that the Base Aircraft must return to starting location to recharge its battery while, as mentioned, the EH Aircraft recharges its battery at the target location.

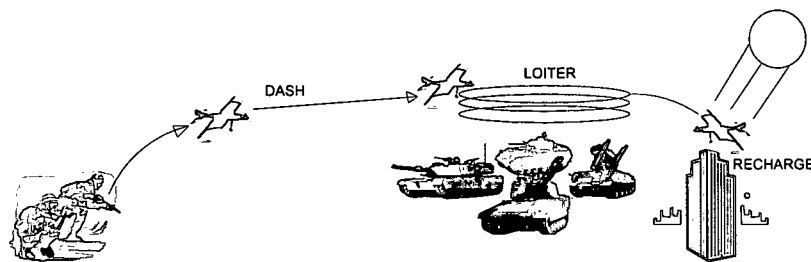


Figure 3.10: EH Aircraft Mission Illustration

3.2.2 Aerodynamic Analysis

A component of the mission simulation is the aerodynamic analysis of the aircraft. To determine the aerodynamic characteristics of the small UAVs the approach provided by Daniel P. Raymer in his third edition of "Aircraft Design: A Conceptual Approach" was used [45]. Although these equations are not meant specifically for aircraft of this size, the aerodynamics of the airplane play a role in the generated entropy. These characteristics, the parasitic drag coefficient C_{D_0} and the lift coefficient C_L , will be required later in the simulation for calculations of entropy, specifically the G term from equation 3.10, and for the simulation itself. The RC aircraft used for this analysis seen in Figure 3.1 was broken down into four components, the wing, fuselage, horizontal tail section, and the vertical tail section.

The C_{D_0} for these components was calculated using the component buildup method.

$$(C_{D_0})_{\text{subsonic}} = \frac{\sum (C_{fi} FF_i Q_i S_{\text{wet},i})}{S_{\text{ref}}} \quad (3.11)$$

where the subscript i represents the different aircraft components, C_f is the skin friction coefficient, FF is the "form factor," Q is the interference factor, S_{wet} is the wetted surface area, and S_{ref} is the reference wing area. The C_f for each component was calculated using equation 3.12 for turbulent flow

$$C_f = \frac{0.455}{(\log_{10} R)^{2.58} (1 + 0.144 M^2)^{0.65}} \quad (3.12)$$

where R is Reynolds number and M is the Mach number. FF was calculated for each of the components using two equations, 3.13 and 3.14 for the wing/tail and fuselage.

$$FF_{\text{wing/tail}} = \left[1 + \frac{0.6}{(x/c)_m} \left(\frac{t}{c} \right) + 100 \left(\frac{t}{c} \right)^4 \right] \left[1.34 M^{0.18} (\cos \Lambda_m)^{0.28} \right] \quad (3.13)$$

Table 3.7: Values for Component Buildup Method at 12 m/s

Component	C_f	FF	Q	S_{wet}	C_{D_o}
Wing	0.0069	0.9173	1.0	0.1070	0.0121
Fuselage	0.0059	1.6658	1.0	0.0335	0.0058
Tail (Horizontal)	0.0069	1.0	1.045	0.0214	0.0027
Tail (Vertical)	0.0079	1.0	1.045	0.009	0.0013
Aircraft	—	—	—	—	.0219

$$FF_{fuselage} = \left(1 + \frac{60}{f^3} + \frac{f}{400} \right) \quad (3.14)$$

where $(x/c)_m$ is the location along the chord (c) of the maximum airfoil thickness (t), Λ_m is the angle of sweep of the maximum thickness line, and f is defined as

$$f = \frac{l}{d} = \frac{l}{\sqrt{(4/\pi)A_{max}}} \quad (3.15)$$

where l is the length of the fuselage and A_{max} is maximum cross sectional area of the fuselage. Since the fuselage is square-sided, the "form factor" was increased by 40%. The interference factor was 1 for every component except the vertical fin and horizontal tail where it was increased 4.5%. The results are tabulated in Table 3.7.

With the parasitic drag coefficient calculated, the coefficients of lift for maximum endurance and maximum range were determined. The C_L for maximum endurance corresponds to the aerodynamic characteristics involving the least amount of power from the engine for flight. It is calculated using equation 3.16

$$C_{L,endurance} = -C_{L_o} + \sqrt{4C_{L_o}^2 + 3C_{D_0}/k} \quad (3.16)$$

where C_{L_o} is the lift coefficient at zero angle of attack given a value of 0 for a symmetric airfoil, and

$$k = \frac{1}{\pi A R e} \quad (3.17)$$

The C_L for maximum range is the coefficient where L/D is a maximum and thus drag is minimized. It is calculated from

$$C_{L,range} = \sqrt{C_{L_0}^2 + C_{D_0}/k} \quad (3.18)$$

For each value of C_L , endurance and range, a correlating velocity was determined. These velocities were then used to define flight characteristics of the mission segments. The velocity associated with the dash segment of the mission simulation is calculated using the $C_{L,range}$.

$$V_{range} = \sqrt{\frac{W_{aircraft}}{1/2 S_{ref} \rho C_{L,range}}} \quad (3.19)$$

where $w_{aircraft}$ is the weight of the aircraft and ρ is the density of the air. The velocity during the loiter period of the mission is calculated similarly as V_{range} with the only difference being the substitution of $C_{L,endurance}$ for the $C_{L,range}$. These values can be determined also by graphing the total drag of the aircraft and the power required to fly the aircraft versus a range of velocities.

3.2.3 Mission Simulation Results

Combining the calculations from the previous sections of this chapter, the EH aircraft and the Base Aircraft were analyzed and compared. For this study, the entropy generated by the solar panels when comparing the the EH and Base Aircrafts is treated in a special way. Looking at Figure 3.11, the same energy from the sun Q_{rad} enters both control volumes. However, the solar cell on the EH Aircraft converts some of the sun's energy into

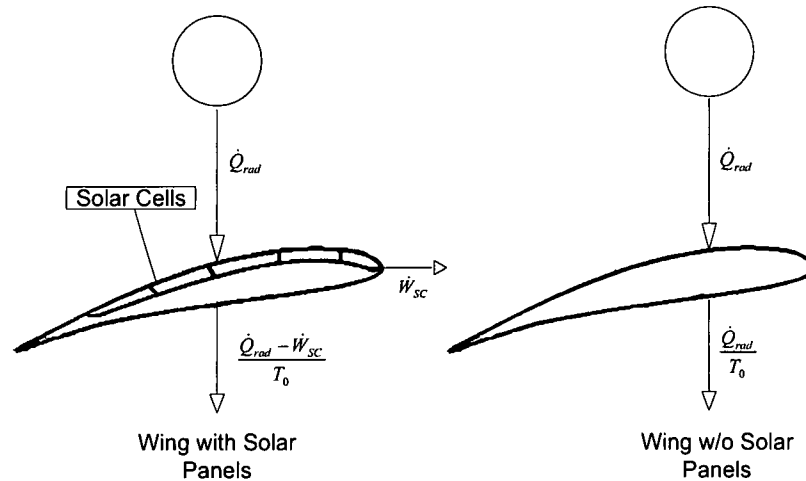


Figure 3.11: S_{gen} Accounting for Solar Cell

power to charge the battery. This power is sent to the charging circuit and is accounted for in the study as a negative entropy generation.

3.2.3.1 Variable Wingspan

The first analysis looks at the effect of the wingspan on the two aircraft. The wingspan of each aircraft was varied from 0.3 to 0.75 meters and the mission simulated for target distances of 0.25, 0.50, 0.75, and 1 miles. The total mission time determined for the simulation, referred to as a "day" previously, was selected to be 12 hours. The environmental inputs needed for the solar array for recharging were selected to be 1000 W/m^2 for ideal sun conditions. The solar panels used for this simulation are Iowa Thin Film Powerfilm[®] P/N MPT 4.8-75 that output 50 milliamps (mA) at 4.8 volts (V) [46]. Figure 3.12 shows the total entropy generated for the entire mission versus the wingspan for the different target distances. These results indicate that the Base Aircraft generates almost 4 times more entropy than the EH aircraft due mainly to the increase time spent dashing to the target. A closer view of the EH Aircraft's total S_{gen} , Figure 3.13, illustrates a sudden increase in total

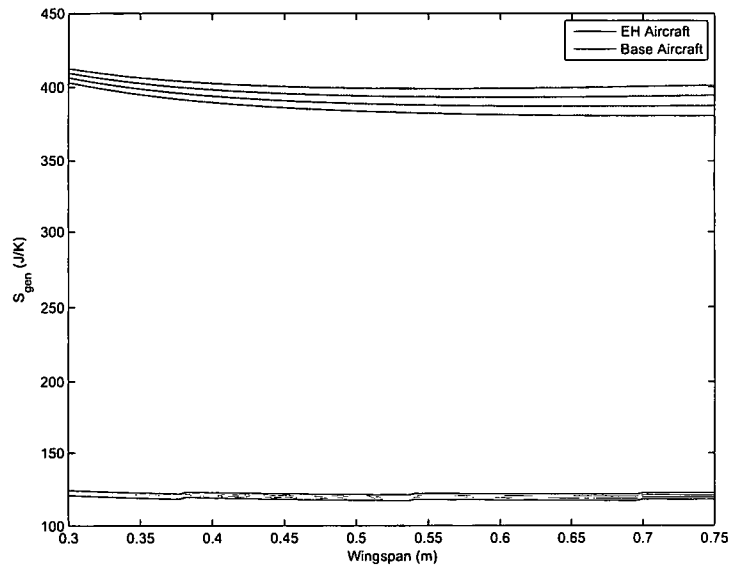


Figure 3.12: S_{gen} for Entire Mission

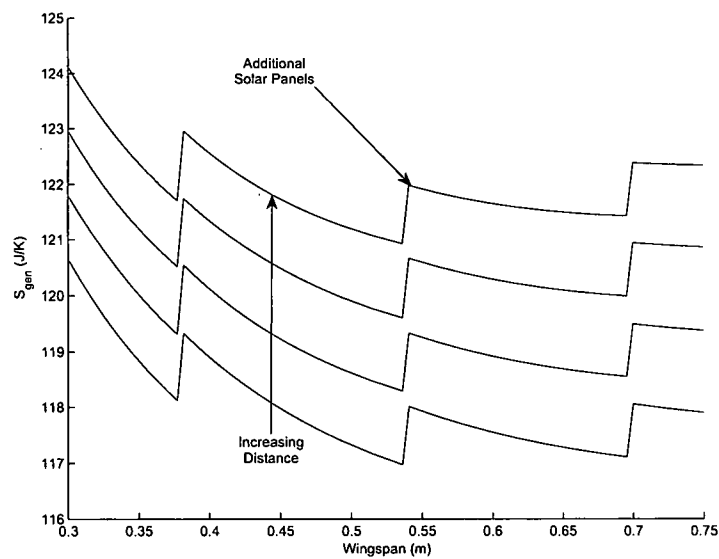


Figure 3.13: S_{gen} for EH Aircraft over Entire Mission

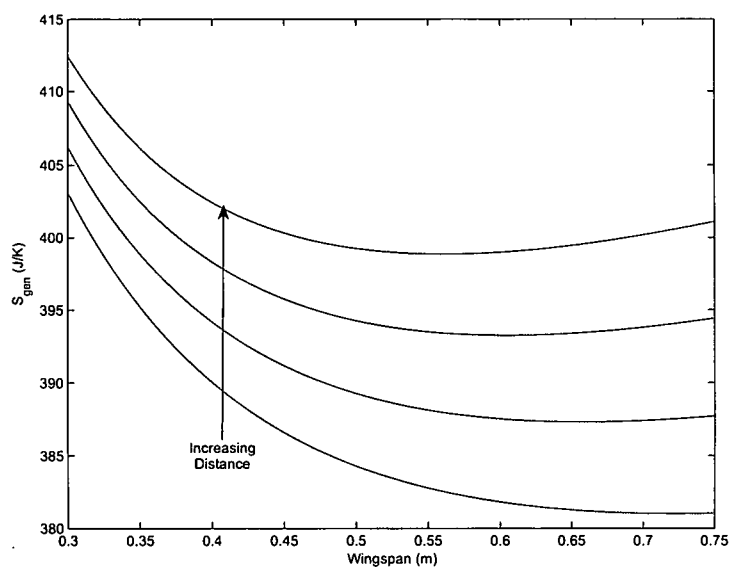


Figure 3.14: Total S_{gen} for Base Aircraft Mission

entropy at around 0.37, 0.55, and 0.7 meters. This increase is due to the to the design of the mission because the solar cells have predefined dimensions and were only added to the aircraft when the wingspan was capable of holding the additional cells. However, noting the scale of the y-axis, this is not a significant effect when compared to Figure 3.12. Observing both Figures 3.13 and 3.14 it can be observed that the total entropy generation increases with increased target distance and as the wingspan decreases. Breaking the mission segments down even further in Figure 3.15, the dash segment shows that the entropy generation increases with target distance for both aircraft. Also of note is that the entropy generated during the dash segment of the mission for the Base Aircraft is affected more so than the EH Aircraft. This is also true for the aircraft's loiter segments as seen in Figure 3.16. The entropy generated in both segments changes as a result of target distance at a much greater rate for the Base Aircraft than that of the EH Aircraft. Furthermore, it is shown in Figure 3.16 that the the total entropy generated in the loiter segments decrease as the target is positioned further away. This is due to the decreased time spent loitering at the target because of the increased energy needed, for the longer dash, from the battery supply. Additionally, the total time spent in the air at the target location shown in Figure 3.17 and demonstrates that for closer targets, the Base Aircraft spends more time in the air at the target location than the EH Aircraft. Figure 3.17 also demonstrates that the Base Aircraft's time spent at the target is affected at a greater rate than EH Aircraft when pertaining to target distance.

From this analysis it can be seen that the wingspan does not have a major effect on the EH Aircraft for the given conditions. For that matter, the distance from the target location does not significantly effect the overall performance during the mission of the EH Aircraft either. On the contrary, the Base Aircraft is affected by both the target distance and wingspan. Looking closely at the total loiter time again in Figure 3.17, as the target distance increases, the total time loitering drops significantly. The reason for such a dramatic drop

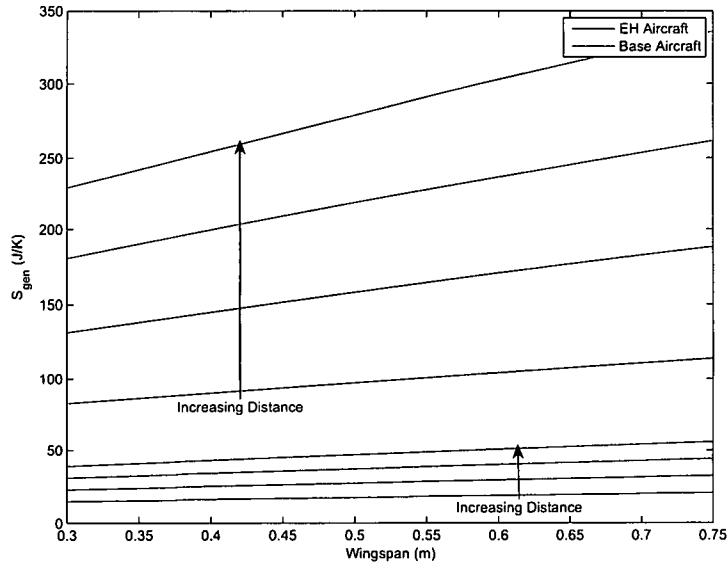


Figure 3.15: S_{gen} for Dash Segment of Mission

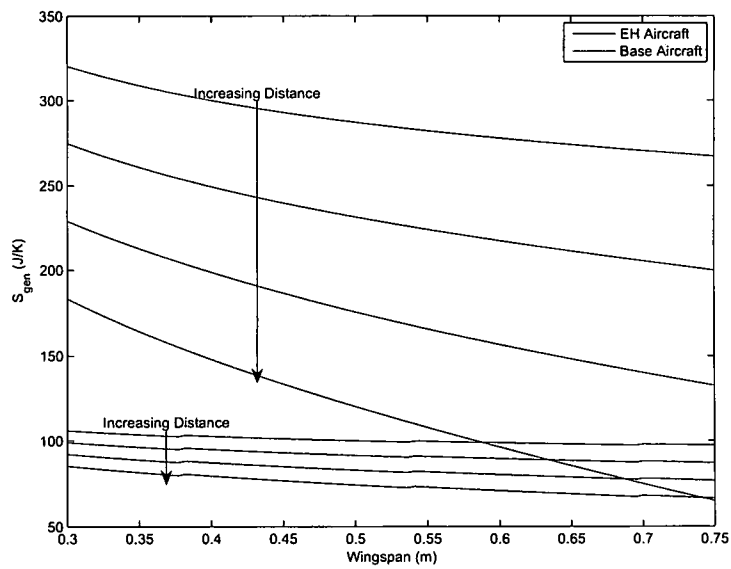


Figure 3.16: S_{gen} for Loiter Segment of Mission

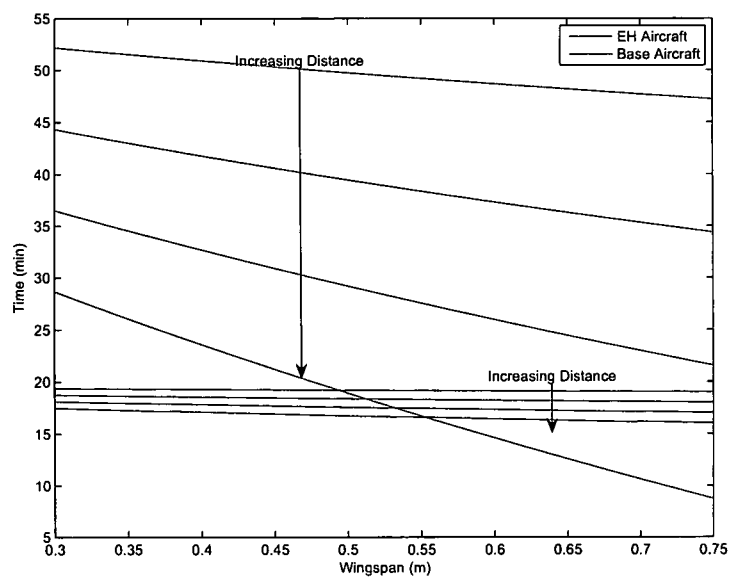


Figure 3.17: Total Loiter Time at Target Location

is the Base Aircraft's dependence on returning to its origin for recharging. It can only fly to the target using half of its initial power as opposed to the EH Aircraft that can use all of its battery power to fly to the target, provided that the target is reachable on a single charge. The wingspan also affects the performance. As the wingspan increases, the Base Aircraft requires more power to dash to the target, thus lowering the amount of time it is able to spend at the target location, whereas the EH Aircraft only has two dashes and is barely affected by the wingspan as mentioned earlier. The next step in the analysis will look at the efficiency of the solar cells.

3.2.3.2 Improved Efficiency Analysis

As research for solar cells improves their efficiency, the performance of the EH Aircraft will also improve. Taking the wingspan analysis approach a step further and examining the mission, simulating a target location 1 mile away, Figure 3.18 shows the mission loiter time for improved efficiencies of the amorphous solar array. The initial 4% amorphous cell is depicted on the graph as analyzed previously as well as the Base Aircraft's performance during the same mission. The additional lines are the times for the improved efficiency of the amorphous cells set at 8, 12, and 20%. This figure demonstrates that for this target distance, the Base Aircraft outperforms the EH aircraft in total loiter time until the efficiency of the amorphous solar cells exceeds 12%.

Monocrystalline solar cells already achieve 12% efficiency. However, they require a support structure due to their brittleness and require some ingenuity mounting them to the EH Aircraft because of the lack of flat space, unlike the flexible amorphous solar cells that can conform to the airfoil. Performing a mission simulation comparing the 12% amorphous cells to the monocrystalline cells shows that the monocrystalline cells offer a small improvement in loiter flight time, as observed in Figure 3.19. However, due to the increased mass of the monocrystalline cells and supporting structure, the EH aircraft with

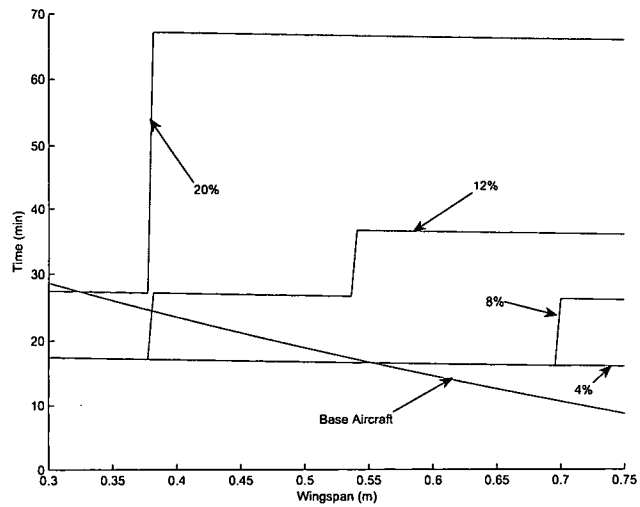


Figure 3.18: Total Loiter Time at Target Location 1 Mile Away for Increasing Efficiencies

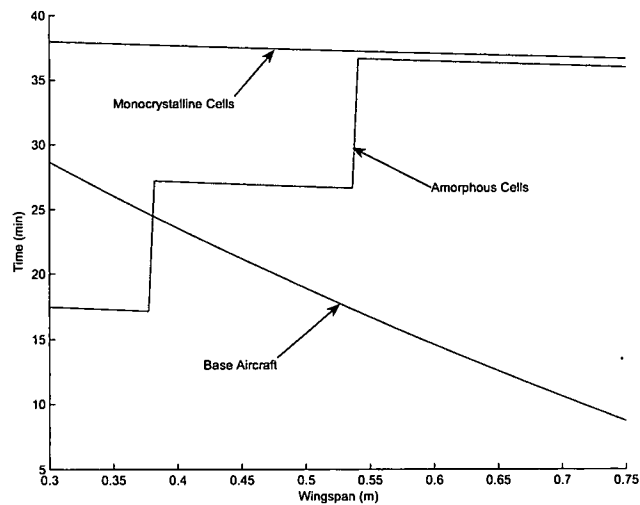


Figure 3.19: Total Loiter Time at Target Location 1 Mile Away for Monocrystalline and Amorphous Solar Cells

monocrystalline cells generates more entropy than the EH aircraft with amorphous solar cells during the dash and loiter segments shown in Figures 3.20 and 3.21.

3.3 Conclusions

This chapter demonstrated that entropy generation can be used as a metric to analyze energy harvesting for small UAVs. The calculations for entropy generation were presented as was an aerodynamic analysis of the Microstick aircraft. For the analysis section, a single flight was analyzed and a mission was designed to compare the Base and EH Aircrafts. The results showed that the motor and propeller generated the highest percentage of total and operational entropy. From the mission simulation, it was concluded that for short target distances the Base Aircraft outperformed the EH Aircraft but produced much more entropy than the EH Aircraft. However, with 12% efficient solar cells, the EH Aircraft exceeded the performance of the Base Aircraft for all target distances.

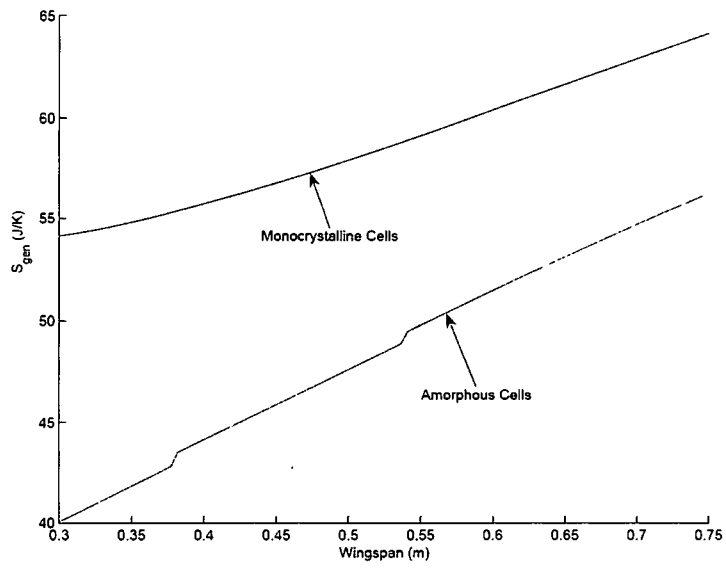


Figure 3.20: S_{gen} for Dash Segment of Mission for Monocrystalline and Amorphous Solar Cells

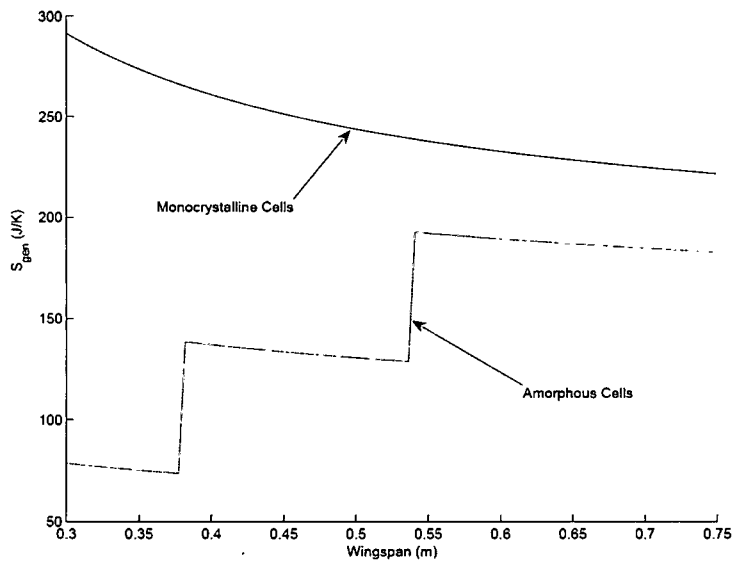


Figure 3.21: S_{gen} for Loiter Segment of Mission for Monocrystalline and Amorphous Solar Cells

Chapter 4

Energy Harvesting Characterization

This chapter will present the characterization for each of the energy harvesting techniques chosen for this thesis. For the solar cells, experimental data will be matched with factory specifications and efficiencies will be determined. Additionally, this chapter will present a simulation model for a piezoelectric bimorph beam and experimental data to verify the model. The data gathered is then used for the development of system level concepts.

4.1 Solar Technology

Solar technology was proven to be a valuable addition for small UAVs under perfect conditions through the use of the mission simulation in the previous chapter. However, the real life performance of the solar cells do not match laboratory specifications provided by the manufacturers. In the following section, two types of solar cells that are readily available will be characterized. These solar cells, monocrystalline and amorphous cells, represent the opposite ends of the performance spectrum and their performance will be tested for various inputs.

4.1.1 Solar Cell Characterization

Performance ratings for solar cells from manufacturers are determined under Standard Test Conditions (STC). These parameters were specified as a radiation intensity of 1000 W/m^2 , a solar cell temperature of 25°C , and an Air Mass (AM) index of 1.5. The Air Mass index is defined as "the intensity and spectral distribution resulting from a certain path length of sunlight through the atmosphere. AM 1 means the sun is directly overhead. AM 1.5 applies at a sun position such that the path length is 1.5 times more" [2]. However, laboratory settings are completely different than one would experience during a day in Ohio or Florida due to the different latitudes and climate conditions. When dealing with a time period of sun up to sun down, the solar radiation, temperature, and Air Mass index change with every hour of the day. To determine the performance of the solar cell throughout the day, the solar cells were characterized using a Daystar Solar Meter, shown in Figure 4.1, and a basic resistance decade box. The Daystar meter has a range of 0 to 1200 W/m^2 with an accuracy of 3% and resolution of 1 W/m^2 . For the characterization test, the solar cells were placed on a level, horizontal surface and connected in series to a load resistance, as seen in Figure 4.2. The test was conducted by changing the resistance of the decade box and recording the voltage and corresponding solar radiation.

The first of the solar cells characterized for this research were monocrystalline cells, designated "Super Cells," and purchased from Solar-World.com. They are rated at 60 mA at 0.5 V for standard test conditions. The second set of solar cells were amorphous cells procured from Iowa Thin Film, Powerfilm[®] P/N MPT 4.8-75, and were the solar cells used in the mission simulation. Their performance rating is 50 mA at 4.8 V. The Powerfilm[®] modules were connected to the load resistance while the the monocrystalline module was doubled in series to produced 60 mA at 1.0 V's.

Each type of solar cell was submitted to varying solar radiation throughout the day.

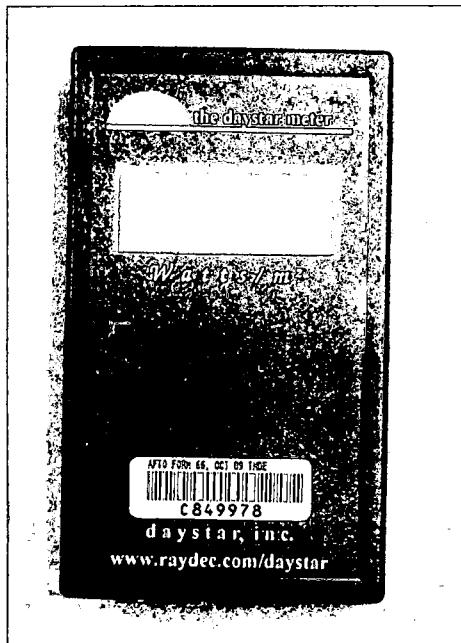


Figure 4.1: Daystar Solar Meter Used in Solar Cell Characterization

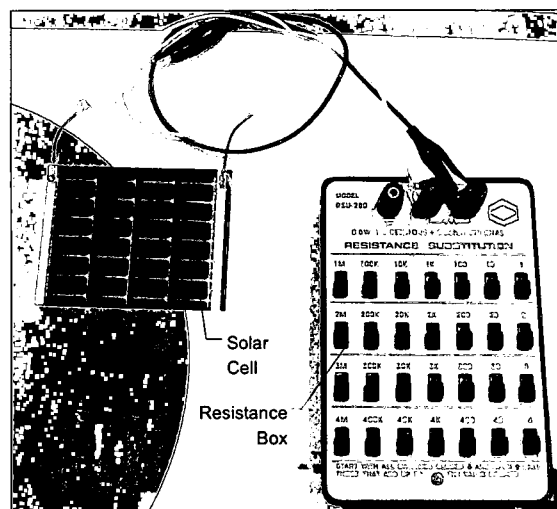


Figure 4.2: Test Setup for Solar Cell Characterization

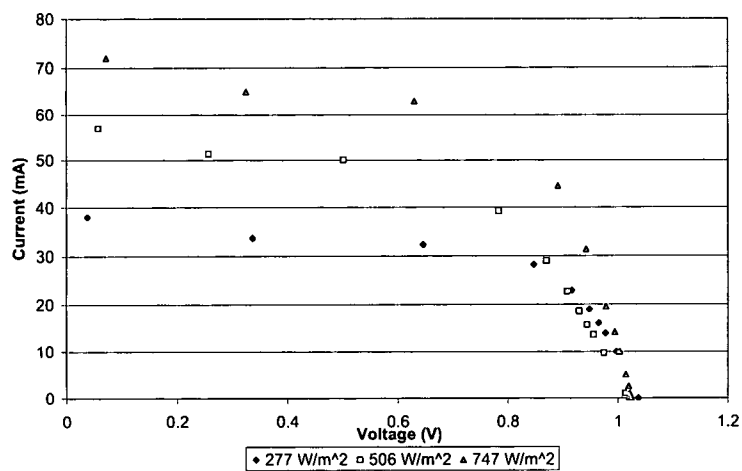


Figure 4.3: Monocrystalline Solar Cell Characterization on August 17th

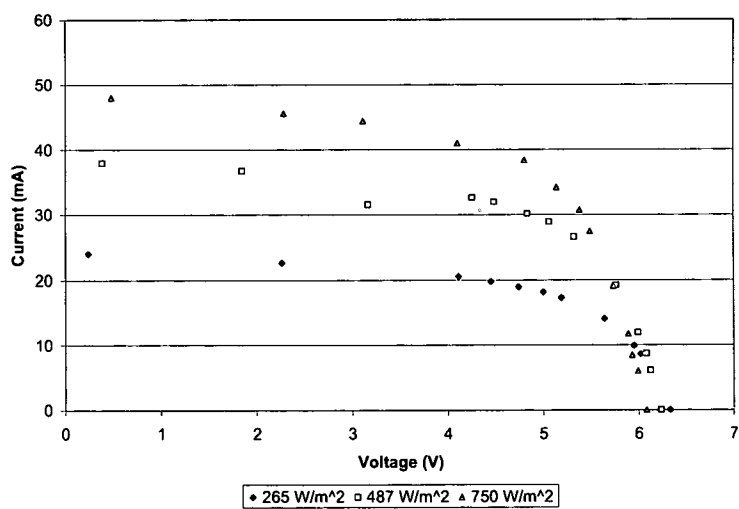


Figure 4.4: Amorphous Solar Cell Characterization on August 17th

Table 4.1: Solar Quality Values

Solar Cell	Peak Efficiency	FF @ 750 W/m ²
Monocrystalline	17.27	0.54
Amorphous	5.72	0.60

Figures 4.3 and 4.4 are the current vs. voltage curves for the solar cells at varied input conditions. The input conditions correspond to the solar radiation at different times of the day, where 277 W/m² corresponds to roughly 9:00 a.m., 506 W/m² was around 10:30 a.m., and 747 W/m² occurred at about 2:30 p.m. on August 1st. The efficiency of the solar cells was calculated using equation 4.1.

$$\eta = \frac{P_{out}}{P_{in}} = \frac{I_m V_m}{Q_{sun} A_{sc}} \quad (4.1)$$

where I_m and V_m are the current and voltage at maximum power, Q_{sun} is the radiation intensity of the sun, and A_{sc} is the area of the solar cell. Another measure of the performance of the solar cell is the fill factor (FF). The fill factor is a ratio of the maximum power output of the solar cell to the open-circuit/short-circuit condition of the solar cells as shown in equation 4.2 and represents how well the IV curve of the solar cell fills the ideal rectangular form [2].

$$FF = \frac{I_m V_m}{I_{sc} V_{oc}} \quad (4.2)$$

where I_{sc} and V_{oc} are the short circuit current and open circuit voltage. The open-circuit voltage corresponds to a circuit with no current flow and the short-circuit current, in turn, corresponds to circuit with no voltage [44]. These values are tabulated in Table 4.1. It can be seen in the table that the monocrystalline cells are roughly 3 times more efficient whereas the amorphous cells fill factor is slightly better.

4.2 Piezoelectric Technology

The use of piezoelectric devices on a small UAV can provide the aircraft with additional power during the harvesting stage but hardly enough to charge a battery compared to solar harvesting. However, solar harvesting is limited to collecting energy only during the day whereas a piezoelectric generator with the right input source can provide power continuously as long as the source vibration is uninterrupted. With the right design and power harvesting circuitry, the use of piezoelectric energy harvesters can be a great supplement to solar harvesting. The next section will provide a detailed look at an analytical model of the piezoelectric bimorph beam.

4.2.1 Piezoelectric Beam Characterization

To understand the general power generation capabilities of a piezoelectric bimorph beam, an analytical model of the beam was developed using the model presented by Sodano et al [47]. Additionally with this model, design concepts for integrated design concepts into the small UAV can be explored. The model was created by starting with the general form of Hamilton's Principle given in equation 4.3

$$VI = \int_{t_1}^{t_2} [\delta T - \delta U + f\delta x]dt = 0 \quad (4.3)$$

where VI is the variational indicator, T is the kinetic energy, U is the potential energy, and $f\delta x$ is the external work done to the system. To construct the model, equation 4.3 must be solved by applying the piezoelectric constitutive equations

$$\begin{Bmatrix} S \\ D \end{Bmatrix} = \begin{bmatrix} s & d \\ d & \epsilon \end{bmatrix} \begin{Bmatrix} T \\ E \end{Bmatrix} \quad (4.4)$$

where S is the strain, D is the electric displacement, s is the mechanical compliance, d is the piezoelectric strain coefficient, ϵ is the dielectric permittivity, T is the stress and E is the electric field. These equations are the reduced three dimensional constitutive equations and in three dimensions, the S and T values are 1×6 matrices and E and D are 1×3 matrices. The three coefficient values, s , d , and ϵ are 6×6 , 3×6 , and 3×3 matrices respectively. Also, three assumptions must be made: the displacement of the beam is a summation of modes in the beam, $\phi(x)$ and a temporal coordinate, $r(t)$, the Euler-Bernoulli beam theory is applied, and the electric potential across the piezoelectric is constant. The final analytical model of the piezoelectric beam is given in equation 4.5

$$\begin{aligned} (M_s + M_p)\ddot{r}(t) + C\dot{r}(t) + (K_s + K_p)r(t) - \Theta C_p^{-1}q(t) &= \sum_{i=1}^{nf} \phi(x_i)^T f_i(t) \\ R\dot{q}(t) - C_p^{-1}\Theta^T r(t) + C_p^{-1}q(t) &= 0 \end{aligned} \quad (4.5)$$

where $M_{s,p}$ are the mass matrices for the substrate and piezoelectric elements of the beam

$$M_s = \int_{V_s} \rho_s \phi^T(x) \phi(x) dV_s \quad (4.6)$$

$$M_p = \int_{V_p} \rho_p \phi^T(x) \phi(x) dV_p \quad (4.7)$$

$$(4.8)$$

where ρ is the density and V is the volume. The terms $K_{s,p}$ are the corresponding stiffness matrices for the substrate and piezoelectric element and are defined as

$$K_s = \int_{V_s} y^2 \phi^T(x) c_s \phi(x) dV_s \quad (4.9)$$

$$K_p = \int_{V_p} y^2 \phi^T(x) c_p \phi(x) dV_p \quad (4.10)$$

$$(4.11)$$

where y is the distance from the center of the beam and $c_{s,p}$ are the modulus of elasticities.

The electromechanical coupling matrix is

$$\Theta = - \int_{V_p} y \phi^T(x) e^T \psi(y) dV_p \quad (4.12)$$

where e is the piezoelectric coupling coefficient and ψ is the field over thickness of the piezoelectric from the third assumption and is constant. The capacitance matrix for the system is calculated using equation 4.13

$$C_p = \int_{V_p} \psi^T(y) \epsilon^S \psi(y) dV_p \quad (4.13)$$

where ϵ is dielectric constant. The $q(t)$ term is the electric charge and $\dot{q}(t)$ is the current.

The force on the beam is a result of its own inertia and is calculated from

$$f(t) = \int_0^L \int_0^b \int_0^t \rho A \omega^2 \sin(\omega t) dz dy dx \quad (4.14)$$

where L is the length of the beam, b is the width of the beam, t is the thickness of the beam, A is the amplitude of the base excitation, and ω is the driving frequency of the excitation.

The damping term, C , was determined using

$$C = \alpha(M_s + M_p) + \beta(K_s + K_p) \quad (4.15)$$

where α and β are determined using the following equation

$$\zeta_i = \frac{\alpha}{2\omega_i} + \frac{\beta\omega_i}{2} \quad (4.16)$$

where $i=1,2,\dots,n$ and ζ_i is determined from the frequency response using the Half Power Method [48]. The next section will discuss the verification of the model experimentally with a piezoelectric bimorph beam.

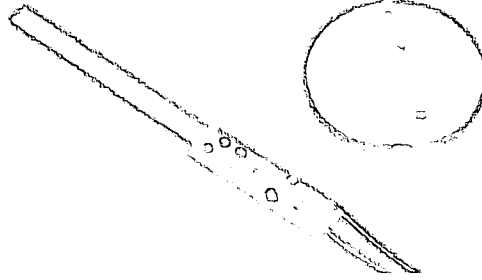


Figure 4.5: Piezo Systems, Inc. Standard Quick-Mount Bending Generator, P/N Q220-A4-103YB

4.2.1.1 Beam Verification

The model presented in the previous section was verified experimentally. The beam chosen to verify the analytical model was a Piezo Systems, Inc. Standard Quick-Mount Bending Generator, P/N Q220-A4-103YB shown in Figure 4.5 [49]. The dimensions and properties of the beam are given in Table 4.2. The experimental setup included a LDS v203 shaker, a Spectral Dynamics Siglab data acquisition system, and a PCB 352C22 accelerometer. To verify that the input to the model was matched to the experimental input, the accelerometer was used to measure the sinusoidal acceleration and the force amplitude was calculated from equation 4.17

$$a = A\omega^2 \sin(\omega t)$$

$$A = \frac{a}{\omega^2} \quad (4.17)$$

where a is the acceleration of the input vibrations. The beam was then subjected to a sweep of input vibrations to determine its frequency response. The results for this are in Figure 4.6 for the experiment and simulation. The simulation for the beam matches the the experimental results pretty well at the first mode. The second mode, however, is not as accurate. The magnitude of the output is acceptable but the frequencies do not

Table 4.2: Piezo Systems Inc. Standard Quick-Mount Generator (P/N Q220-A4-103YB) Dimensions and Properties

Property	Value
L	28.6 mm
b	3.2 mm
t	0.508 mm
C_p	15 nF
Tip Deflection	± 0.63 mm
K_3^T	1800
d_{31}	-190×10^{-12} m/V
c_s	111 GPa
c_p	68 GPa
ρ_s	8300 kg/m ³
ρ_p	7600 kg/m ³

match. This could be due to the damping coefficients calculated for the higher modes not being accurate. Therefore, the code will only be used to look at the first mode frequency verifications of the beam for future tests. The voltage and current outputs across a 17.4k Ω resistor are presented in Figures 4.7 and 4.8. Each of the figures show that the simulation and the experiment match closely to one another. From this data, it is reasonable to say that the analytical model of the beam provides accurate results and can be used for other simulations.

4.3 Chapter Summary

This chapter presented basic characterizations of the energy harvesting technologies chosen for this thesis. It was seen that the solar cells do not meet their factory specifications but as the input reaches a full sun, 1000 W/m², the power output is reasonably close. The efficiencies were determined for the two types of solar cells and it was verified that the monocrystalline cells were the more efficient at roughly 17%.

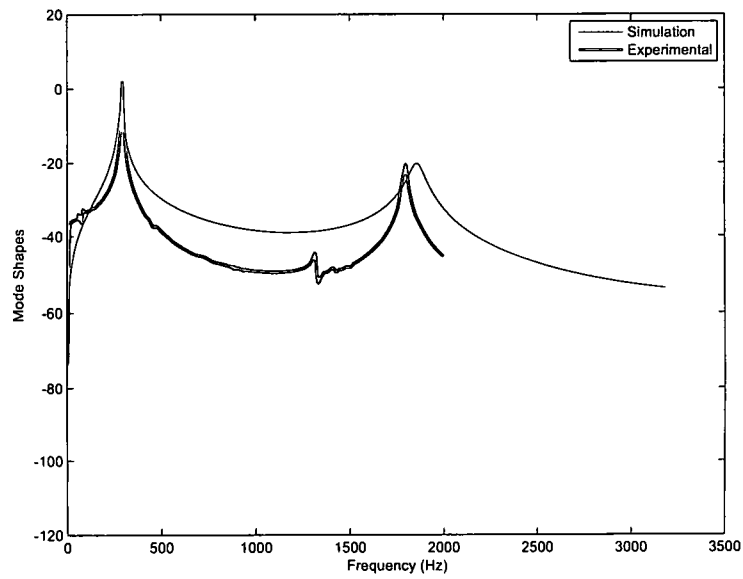


Figure 4.6: Frequency Response From the Experiment Compared to the Analytical Model

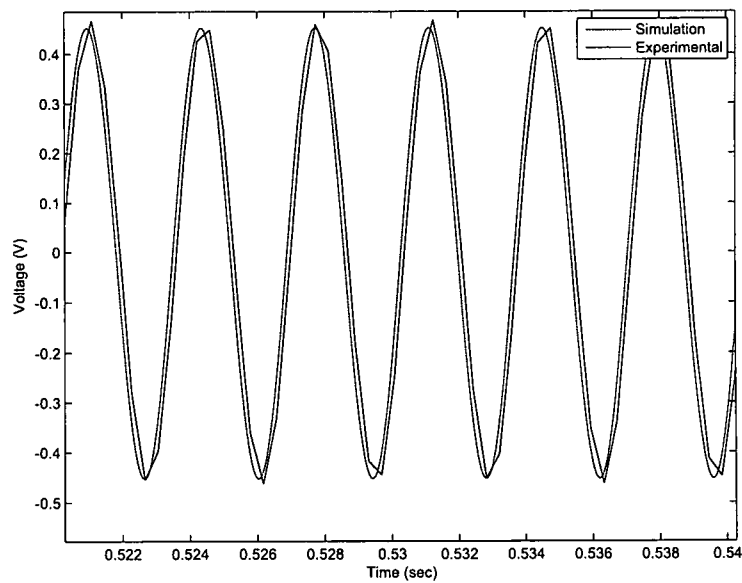


Figure 4.7: Voltage Output of the Beam Generator at 295 Hz across a 17.4 kΩ Resistor

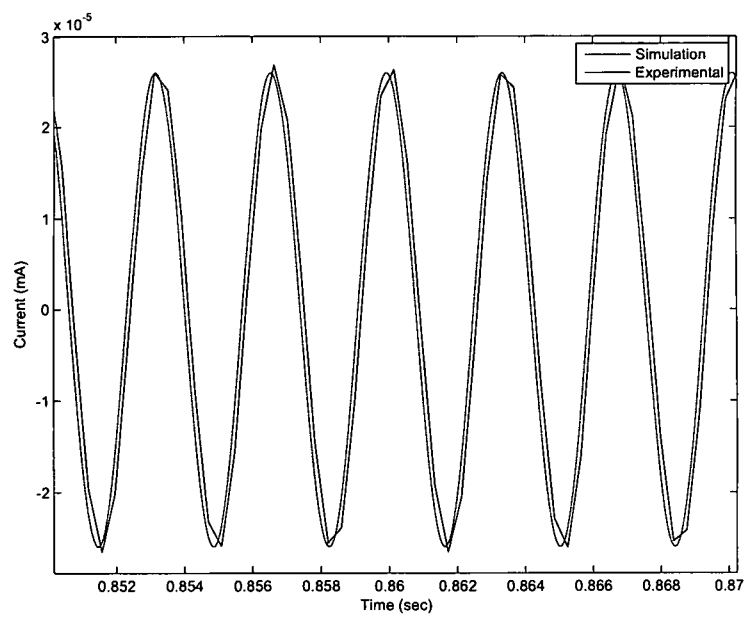


Figure 4.8: Current Output of the Beam Generator at 295 Hz across a 17.4 k Ω Resistor

Also, an analytical model of the Piezo Systems Inc. bimorph beam was created and verified experimentally to be used in the next chapter. The outputs of the beam were given and showed that the piezoelectric beam generator produced substantially lower amounts of power compared to the solar cells. The next chapter will use this information to provide ideas for integrating the energy harvesting technologies into the small UAV.

Chapter 5

Energy Harvesting Integration

In this chapter designs will be presented for the integration of the solar cells and piezoelectric devices as energy harvesters for a representative small UAV. The solar cell concept will be implemented and analyzed for the wing of the aircraft while the piezoelectric concepts will involve integration into the landing gear. Analytical and experimental tests were created to study the performances of the designs for the small UAV system.

5.1 Solar Harvesting

The wing of the Micro Stick aircraft provides the most area for solar cells. Between the two types of solar cells tested in the previous chapter, the amorphous cells provide the better solution for solar energy harvesting of the small UAV scale. Even though the amorphous cells produce the lower power per square meter, their flexibility is a major advantage, capable of wrapping around a 2 in. cylinder as illustrated in Figure 5.1. This provides the advantage of conforming to an airfoil as shown in Figure 5.2. The monocrystalline cells, with their rigidity and brittleness, create a problem associated with placement on the small UAV. Due to the size of the aircraft, there are few flat spaces to place these cells and special manufacturing would be needed to produce a curved monocrystalline cell to match the airfoil being used on the aircraft, in turn increasing the cost of manufacturing. Another possible solution for monocrystalline cells would involve placing them inside the airfoil and use

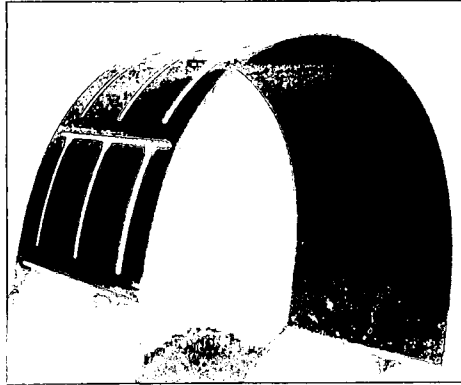


Figure 5.1: Flexible Amorphous Solar Cell

a clear aircraft skin. However, the creation of shadows from the structure and the resulting shadow effect produces additional problems. The shadow effect is the degradation of the power output of the solar array because the array responds to the worst cell in the group [3, 2]. To avoid this problem, either translucent spars and ribs would need to be used to let light pass through them to the cells or bypass diodes would need to be implemented in the series connected solar cells in the array if clear structural members were not used [2]. Using the bypass diodes alleviates the shadow effect but lowers the total power output of the array. Therefore, due to the complexity of the integrating monocrystalline solar cells into the design, the amorphous solar cells will be implemented into the system.

For this study, the amorphous solar cells that were used to create the solar array were Powerfilm[®] MPT6-75 cells. Although these cells were different than the solar cells characterized in the previous chapter, they are the same amorphous solar cell technology and still roughly 5% efficient. Also, these cells were chosen because of their higher power output, 50 mA at 6 volts, and due to the circuit used for charging the lithium polymer battery of the Micro Stick airplane. Lithium polymer batteries require a special circuit that charges the battery in a constant current, constant voltage sequence. The charging circuit implemented in the design was a Maxim Integrated Products MAX745EVKIT switch mode

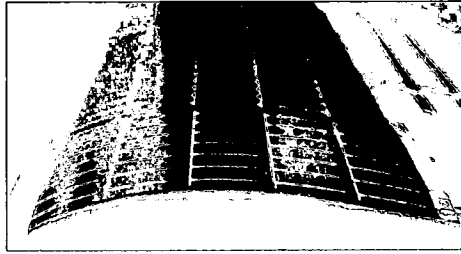


Figure 5.2: Amorphous Solar Cells Conforming to Airfoil

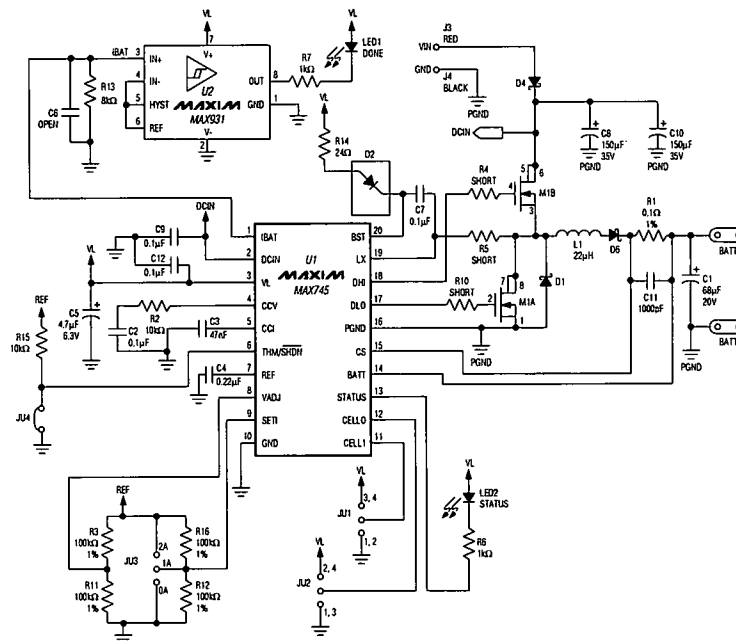


Figure 5.3: Maxim Integrated Products MAX745EVKIT Switch Mode Lithium Ion Battery Charging Circuit [6]

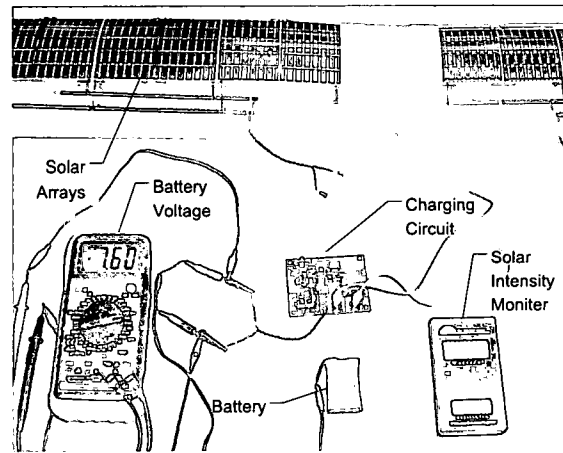


Figure 5.4: Test Setup for Charging Batteries

lithium ion battery charger displayed in Figure 5.3. It is capable of charging lithium polymer batteries with 1-4 cells and requires input voltages between 6-24 volts [6]. As shown in the previous chapter, when the solar intensity decreases, so does the output voltage and current of the solar cell. Therefore, the cell with the highest power output capable of fitting on the small UAV wing was selected to allow for a greater range of solar intensities while still being above the required battery voltage. The higher input from the solar cells will then result in faster charging times.

The test setup for the battery charging test is shown in Figure 5.4. It consists of a solar array mounted to an arbitrary airfoil, a voltmeter to determine the battery voltage, the MAX745EVKIT circuit, the Daystar solar intensity meter, and a lithium polymer battery. Testing of the solar array and the charging circuit consisted of placing the solar array in the sun and monitoring the battery voltage. The battery used for this test was a 8.4 volt 340 mAh 2 cell lithium polymer battery. Once the battery was charged, which was determined by waiting until the battery voltage was constant for 10 minutes, the battery was connected to the Micro Stick aircraft. The engine was then operated at roughly 1/2 throttle, to simulate flying, until the battery reached the cutoff voltage limit in the electronic speed controller.

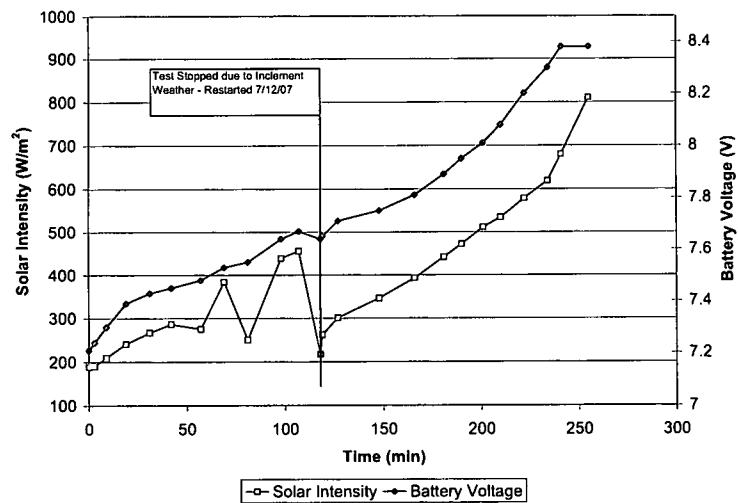


Figure 5.5: Battery Charging Starting at 8:30 a.m. on July 10th and Restarted on July 12th at 9:00 a.m. Due to Inclement Weather

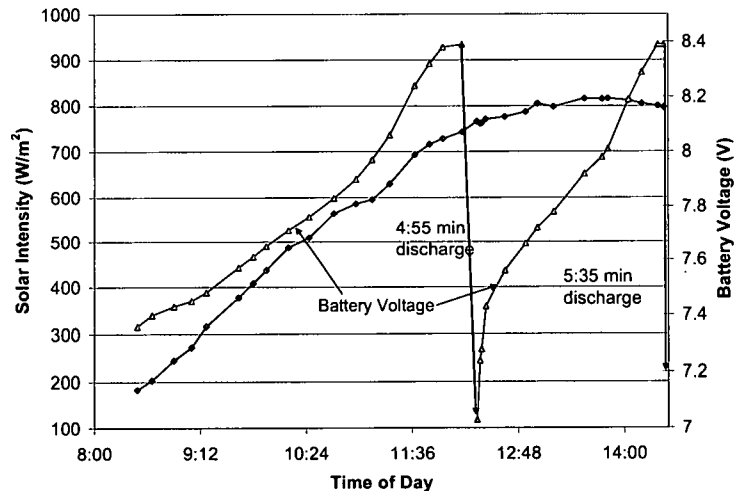


Figure 5.6: Battery Charging Starting at 8:30 a.m. on August 1st Showing 2 Discharges

To verify that the solar array would perform as expected, charging tests were conducted at various times of the day. Figure 5.5 shows a test starting in the morning and stopped in the middle of the test because of cloud cover. The test was restarted 2 days later. It demonstrates that the charging can take place at two different times and will charge as long as there is enough sunlight. In Figure 5.6, two charges were conducted back to back to simulate the small UAV during a mission. The battery was discharged at 8:30 a.m. and connected to the charging circuit. Once fully charged, the battery was discharged again and placed on the circuit again. Since the battery capacity was 340 mAh, which is smaller than the battery that was used in the mission simulation, the times for this test are much shorter. The discharges, or flight times, were about 5 minutes and is the same discharge time for a battery being charged with plenty of power. For a projected day, the battery should be able to charge an additional two times resulting in 25 total minutes of flight time.

This design shows that for the given wing configuration, the solar panels were capable of charging the battery. The charging circuit also performed as desired and is small

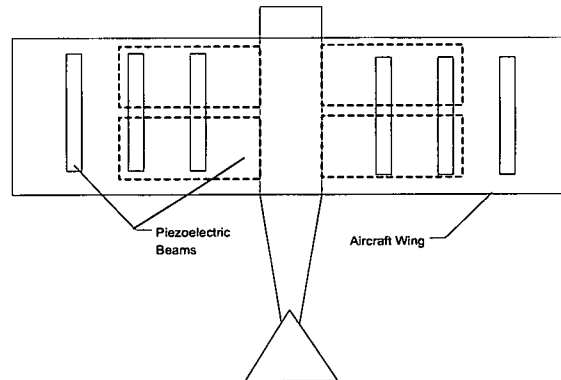


Figure 5.7: Initial Design for Piezoelectric Generators Inside Wing Structure

enough to be implemented into the small UAV. Finally, these tests prove that the small UAV could land and recharge its batteries for additional flight time, making solar energy harvesting a worthwhile addition.

5.2 Mechanical Vibration Harvesting

Integrating piezoelectric benders into the small UAV is the first step into determining their potential usefulness on the aircraft. Using mechanical vibration harvesting provides the aircraft with an alternative to solar harvesting. It could be used to supplement the solar power or provide power to its own sensor on the aircraft. The initial idea was to integrate an array of piezoelectric benders into the the wing structure as illustrated in Figure 5.7. However, after some consideration, it was determined that much of the energy from the vibrations would be lost through the structure of the aircraft. The solution was then to get the piezoelectric generators as close to the source vibrations as possible. The closest possible location was the landing gear and therefore, ideas for replacing the landing gear with piezoelectric generators were designed and analyzed. In the following sections, two landing gear designs will be discussed.

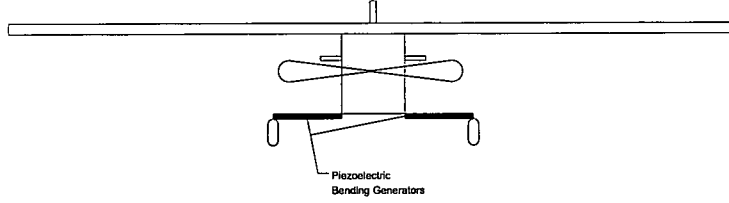


Figure 5.8: Illustration of Cantilevered Piezoelectric Beam Used as Landing Gear

5.2.1 Cantilevered Landing Gear

The first design for the piezoelectric landing gear involves mounting a cantilevered piezoelectric bimorph beam off of the connection to the vibration source and using the aircraft as a tip mass. An illustration of this design is shown in Figure 5.8. To analyze the design, the analytical beam model from the previous chapter was altered for the inclusion of a tip mass. The addition of the tip mass involves two changes, the mass matrix and the force interaction term. To account for the tip mass, the substrate mass was changed to

$$\dot{M}_s = \int_{V_s} \rho_s \phi^T(x) \phi(x) dV_s + M \phi^T(L) \phi(L) \quad (5.1)$$

where M is the tip mass, the mass of the aircraft in this analysis, and $\phi(L)$ is the mode shape at the tip of the beam [48]. The force interaction term included the additional effects of the tip mass by adding $M_a \phi^T(L)$ to $f(t)$ as shown in equation 5.2

$$f(t) = \int_0^L \int_0^b \int_0^t \rho A \omega^2 \sin(\omega t) dz dy dx + M_a \phi^T(L) \quad (5.2)$$

The initial tip mass for this study was determined by dividing the mass of the aircraft, approximately 150 grams, by two. The first iteration of adding the tip mass to the same beam from the analytical model showed that the natural frequency of the system was reduced from 295 Hz to 10 Hz. This is shown in Figure 5.9. The problem arises that most environmental vibration sources are between 60 and 200 Hz with an acceleration of 0.1 to

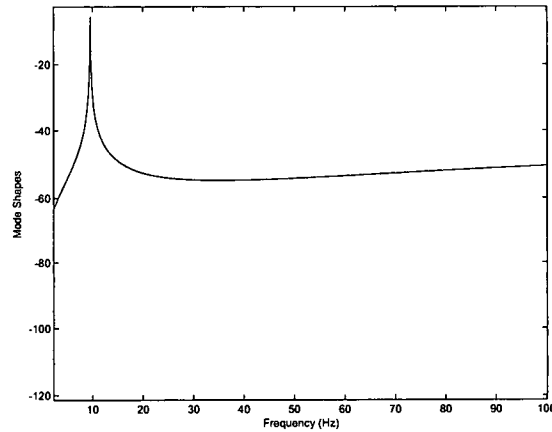


Figure 5.9: Frequency Response of Piezo Systems Beam

10 m/s² [20, 50]. Therefore the beam verification model was modified to study the size of the beam and its effects on the natural frequency.

To analyze the natural frequency of the cantilevered beam for this design the length and width of the beam were varied. For an aircraft mass of 75 grams, Figure 5.10 shows that the natural frequency of the beam does not reach 60 Hz for the prescribed lengths and widths. It does move towards the higher frequencies as the length of the beam gets shorter, however, the highlighted point on the graph is for a 1 cm long beam. Going beyond this mark is not reasonable for this design because as shown in Figure 5.11 the power at this size beam is roughly 0.5 mW and sloping to zero. To raise the natural frequency of the system, the tip mass was changed to 50 grams and then 25 grams, which accounts for additional cantilevered landing gear and not a smaller aircraft. Only when the tip mass was 25 grams was the natural frequency above 60 Hz as shown in 5.12. Again even at this frequency the power output is still low at 0.15 mW but does increase as shown in 5.13. However, as observed in both Figures 5.11 and 5.13, at lower frequencies the power output of the piezoelectric generators are significantly higher. Therefore, it appears that the cantilevered gear would be beneficial to implement into the system if the vibration source

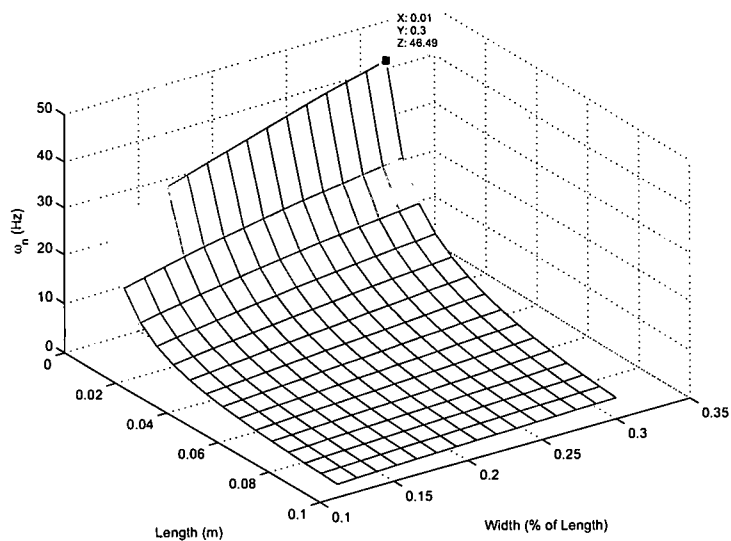


Figure 5.10: Natural Frequency of Modeled Beam with 75 gram Tip Mass

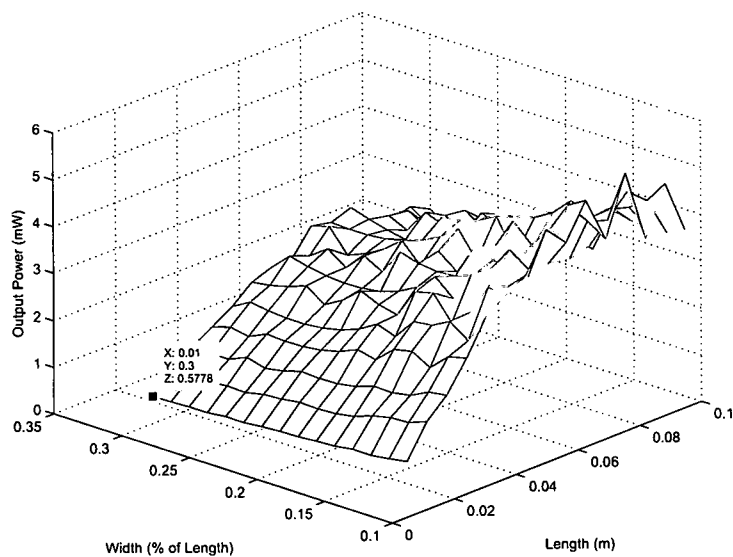


Figure 5.11: Power Output of Modeled Beam with 75 gram Tip Mass

was known to be smaller.

5.2.2 Curved Beam Landing Gear

The second design considered for adding piezoelectric devices as energy harvesters was to place the aircraft on curved beams as depicted in Figure 5.14. Since the analytical model mentioned previously was only developed for a cantilevered beam, the curved beam design was analyzed experimentally. The curved beam used during testing was a Face International Corporation Thunder[®] Actuator TH-8R as shown in Figure 5.15 with the ends of the beam bent to support a mass and connect to the vibration source. To simulate the mass of the aircraft in the experiment, metal washers were attached to the top surface of the beam.

The test setup for the curved beam analysis is shown in Figure 5.16. It consists of a Labwork Inc. pa-138 power amplifier, a Labwork Inc. ET-132-2 shaker, an Agilent 33220A 20 MHz Function/Arbitrary Waveform Generator, a PCB Piezotronics 352C22 accelerometer, a Datastick[®] Systems Inc. VSA-1212 Vibration Spectrum Analyzer Module and Garmin iQue[®] 3200, a voltmeter, and a resistance box. A closeup of the curved beam is given in Figure 5.17 and shows the metal washers sitting upon the curved beam simulating the aircraft mass.

The test was designed to look at two different aircraft masses while varying the input acceleration at approximately the natural frequency of the system. The masses tested were roughly 50 and 75 grams to simulate one third and one half of the aircraft mass. The input acceleration was changed from 5.5 m/s^2 to 10 m/s^2 . The first figure, 5.18, is the data from the 5.5 m/s^2 acceleration input. The natural frequency for the system decreased as more mass was added to the system from 145 Hz for the 50 gram mass to 120 Hz for the 75 gram mass. It is also noted that the peak power output increases nearly 6 times with the increase in mass from 0.5 mW to 2.9 mW. Figure 5.19 demonstrates that as the input

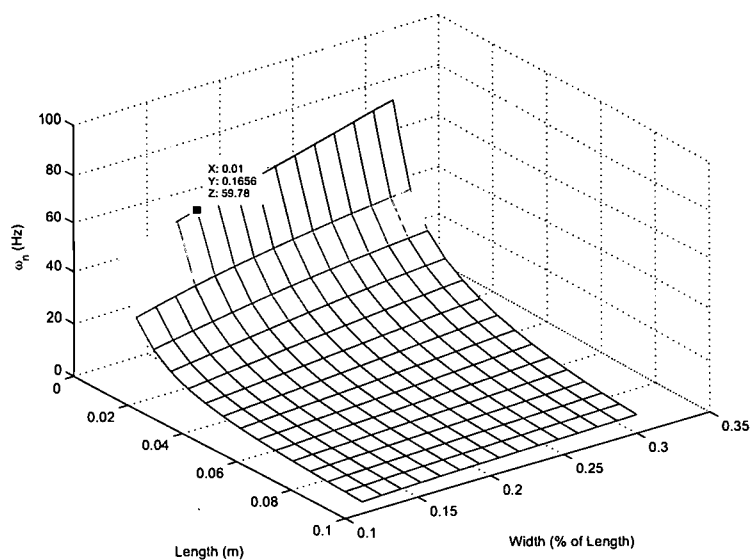


Figure 5.12: Natural Frequency of Modeled Beam with 25 gram Tip Mass

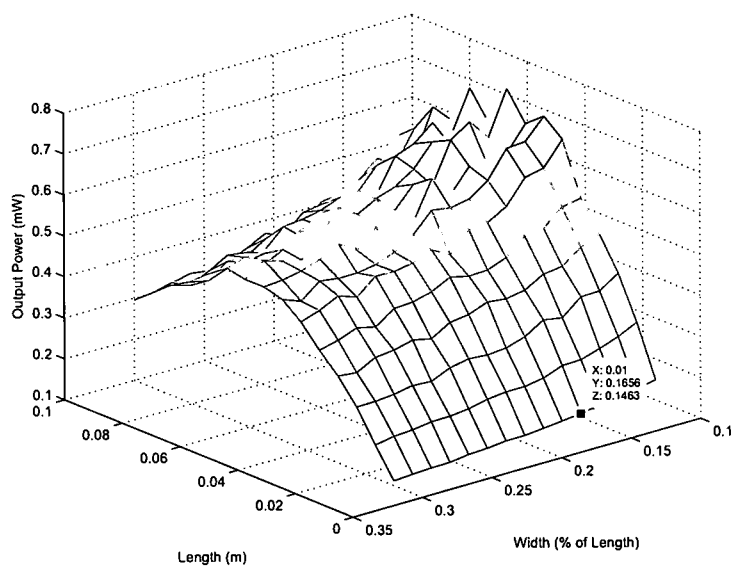


Figure 5.13: Power Output of Modeled Beam with 25 gram Tip Mass

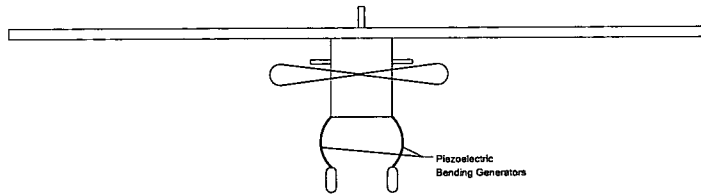


Figure 5.14: Illustration of Curved Piezoelectric Beam Used as Landing Gear



Figure 5.15: Face International Corporation Thunder[®] Actuator TH-8R Curved Beam

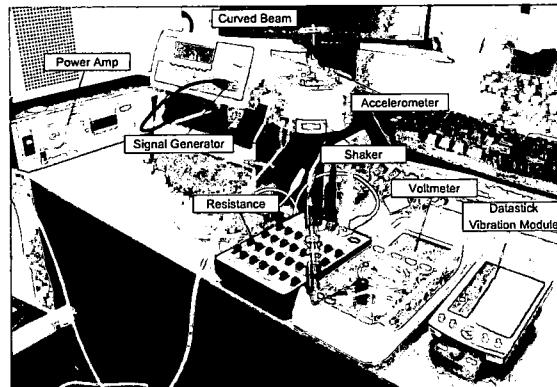


Figure 5.16: Test Setup for Curved Beam Landing Gear

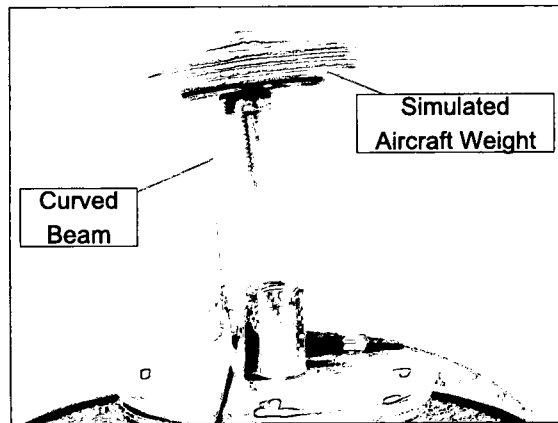


Figure 5.17: Closeup of Curved Beam Landing Gear

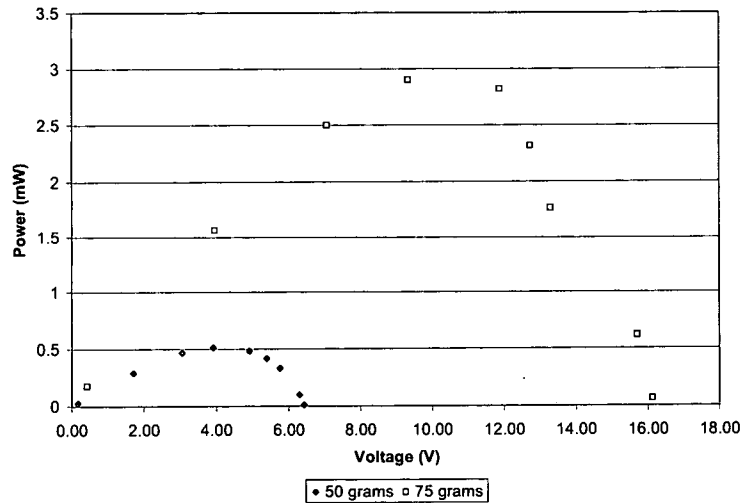


Figure 5.18: Curved Beam Output at 5.5 m/s² for Two Simulated Aircraft Masses

acceleration increase to 10 m/s² the peak power outputs increase substantially for both masses to 1.1 mW and 5.7 mW.

Comparing the curved beam design to the cantilevered beam design, in Figure 5.20 it can be observed that for similar inputs, the cantilevered design has the higher power outputs but only at low input frequencies. As the input frequency is increase, the curved beam outperforms the landing gear design and is better suited for the frequencies in the environment. From this data, it is shown that the curved beam system, although producing low power, can be integrated into the aircraft structure to produce enough usable power to aid the small UAV during its mission at high frequencies.

5.3 Conclusions

This chapter introduces designs for integrating solar and mechanical energy harvest- ing into the small UAV. Tests were conducted for the solar energy harvesting that showed that charging batteries with solar power at this scale is feasible. Integrating the piezoelec- tric generators into the structure required a little more ingenuity and designs for piezo-

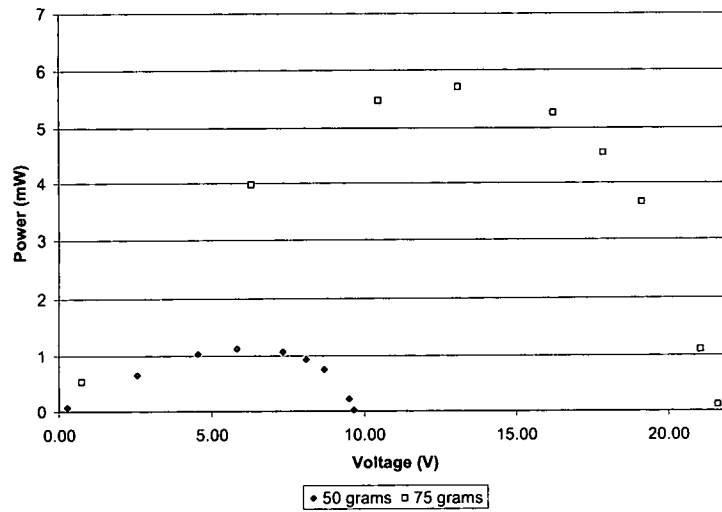


Figure 5.19: Curved Beam Output at 10 m/s² for Two Simulated Aircraft Masses

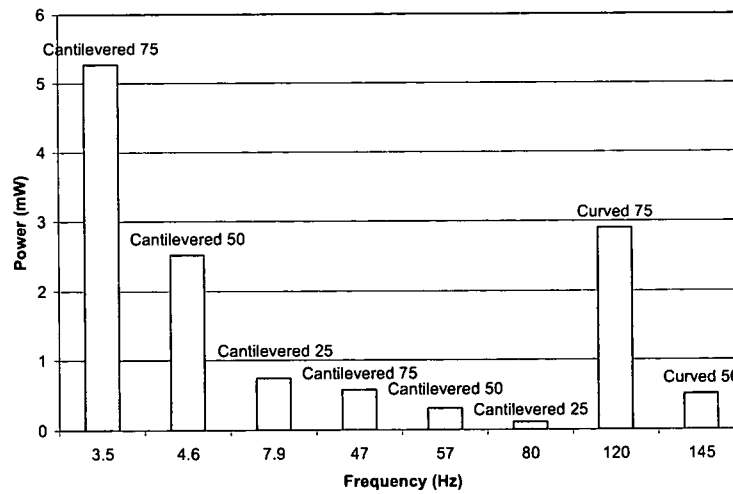


Figure 5.20: Maximum Power Outputs at Natural Frequency of Model Landing Gear

electric landing gear were presented and analyzed. Of the two designs, the cantilevered landing gear and curved beam landing gear, the curved beam landing gear performed better, being capable of operating at frequencies found in the environment with reasonable power outputs.

Chapter 6

Conclusions and Recommendations

6.1 Energy Harvesting for Small UAVs

This thesis investigated the addition of energy harvesting for a small UAV. The initial investigation involved an analysis of the small UAV using the 2nd law of thermodynamics with entropy generation as a metric for evaluating the small UAV. Entropy generation calculations were then presented for the individual components of the UAV. With these calculations, a single flight of the UAV was analyzed to determine the sensitivities of the efficiencies of the aircraft components while also examining the total entropy generated by each of the components. The sensitivity analysis varied the efficiencies of the components and showed that the electric motor and propeller caused the total entropy to change more rapidly based on their efficiencies. Also exploring the entropy generated, it was found that the motor and propeller also generated the most entropy due to the fact that they are the least efficient parts of the aircraft system.

With the entropy generation calculations figured for the small UAV, the analysis was furthered by examining the aircraft over a longer period of time to account for the addition of the energy harvesting. A reconnaissance mission was developed to compare the energy harvesting aircraft to a non energy harvesting aircraft to determine their performances. The energy harvesting aircraft used solar cells to recharge its batteries while still at the target location. The development of the mission also involved determining the

aerodynamic characteristics of each aircraft. For the mission presented, each aircraft's performance was analyzed for target distances that increased in length and also for different aircraft geometries. The first analysis of the two aircrafts showed that the energy harvesting aircraft generated much less entropy but was unable to stay in the air at the target as long as the non energy harvesting aircraft. This was due to the increased time for recharging the batteries of the energy harvested because the power output of amorphous solar cells was low for the specific aircraft geometry. However, as the target distance increased, the performance of the two aircraft began to converge. The mission simulation also analyzed the improvement in technology for the amorphous solar cells and the performance of monocrystalline cells on the energy harvesting aircraft. This analysis showed that for solar cells above 12% efficiency, the energy harvesting aircraft will outperform the non energy harvester. Between the two types of solar cells, it was determined that the monocrystalline cells could fly longer at the target but generated more entropy due to the increase mass needed to support them.

After the mission simulation, two types of energy harvesting technologies were selected and characterized. The two technologies were solar energy harvesting and mechanical energy harvesting using piezoelectric materials. To characterize the solar energy harvesting, a solar meter was used to determine the solar radiation of the sun and the solar cells were connected to an electrical resistance to determine the maximum power of the solar cell. For the two types of solar cells, monocrystalline and amorphous, the monocrystalline exhibited more than three times the efficiency of the amorphous cells. The characterization of the piezoelectric devices involved creating an analytical model of a piezoelectric bimorph beam. To verify the analytical model, the results of an experimental test were used and it was determined that the model was accurate for the first mode of the beam.

This thesis then analyzed system level designs for the integration of the energy harvesting devices. The use of solar cells on an airfoil was analyzed for charging a battery. Charging tests were conducted by placing the solar array in the sun and charging a lithium polymer battery with successful results. Furthermore, two types of piezoelectric generator designs were presented. The piezoelectric generators replaced the landing gear with cantilevered and a curved beam designs. The results showed that the cantilevered design was more suitable for lower frequency input vibrations and that the curved beam design was the better of the two. These two designs with the inclusion of the solar array were successfully demonstrated to be beneficial for a small UAV.

6.2 Recommendations

The use of piezoelectric and solar technology for small UAVs proved to offer enough power for applications of this size. Future work should include developing circuitry that will be able to recharge the battery of the small UAV and act as the speed controller for the electric motor. Additionally, the circuitry should be designed to accept the power from a piezoelectric generator to charge the battery or a sensor. Furthermore, the piezoelectric landing gear generators presented should be implemented into the small UAV and tested in the environment.

Appendix A

Entropy Generation

A.1 Aircraft Control Volumes

The first figure, Figure A.1, shows the work rates and heat rates that are used in determining the entropy generation for the subsystems. The next figure, Figure A.2 is a detailed look at the energy harvesting additions for the aircraft. The piezoelectric device is shown for informational purposes only and is not included in the calculations for this thesis analysis.

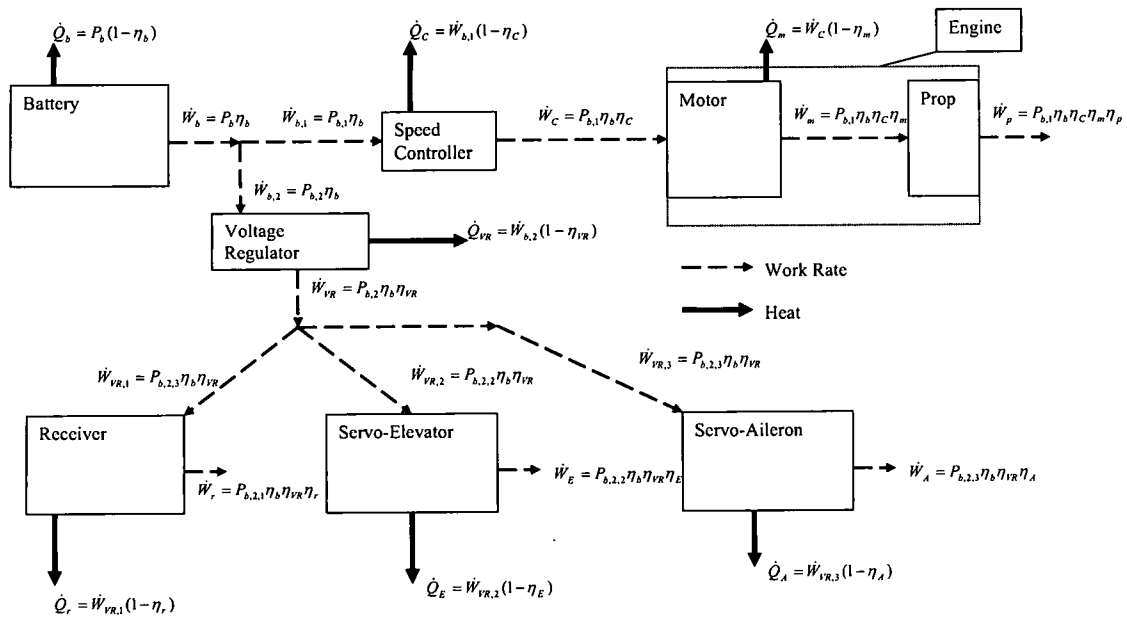


Figure A.1: Control Volume With Detailed Work and Heat Rates

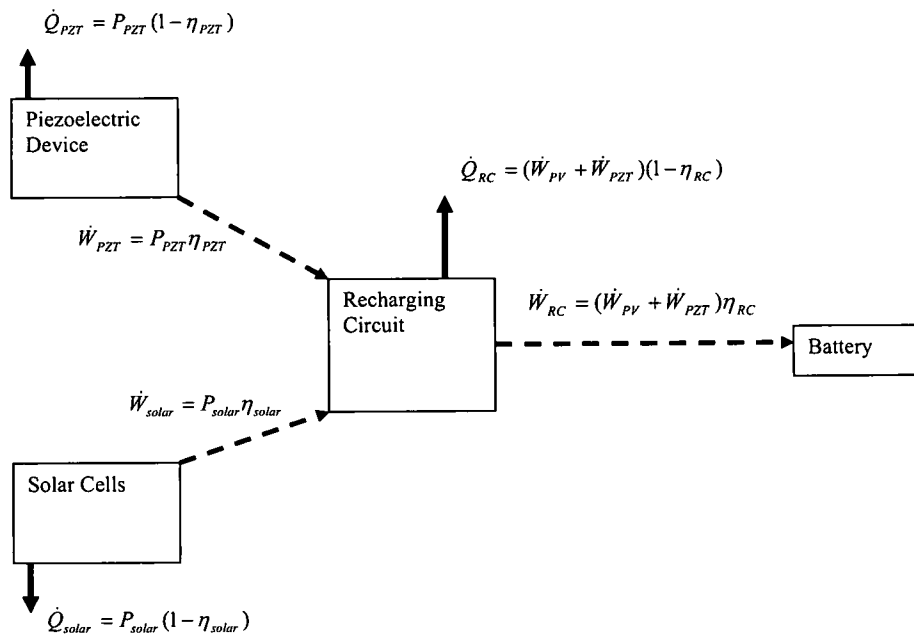


Figure A.2: Energy Harvesting Additions

Appendix B

Additional Solar Cell Characterizations and Battery Charging Tests

The following figures provide the data for additional solar cell tests that were not presented previously.

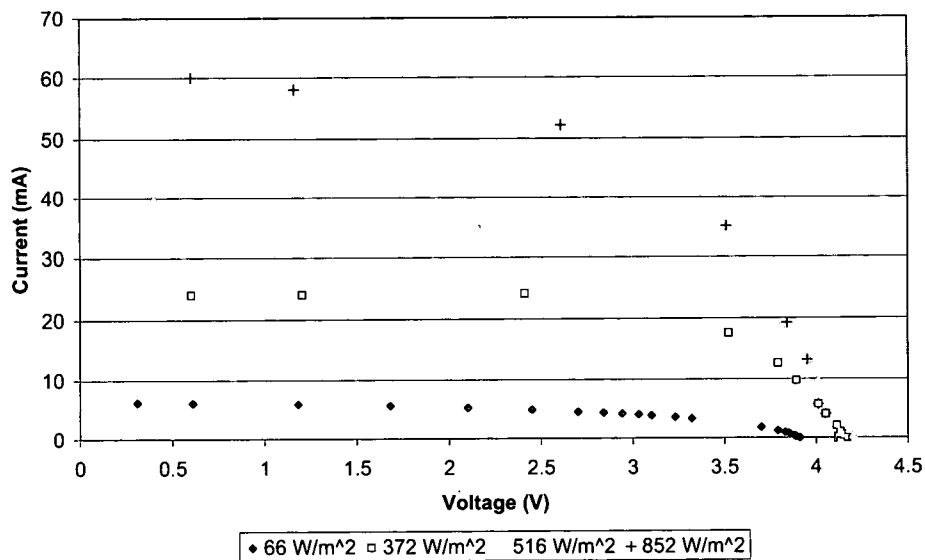


Figure B.1: Solar Cell Characterization for Powerfilm® MP3-37 on May 24th

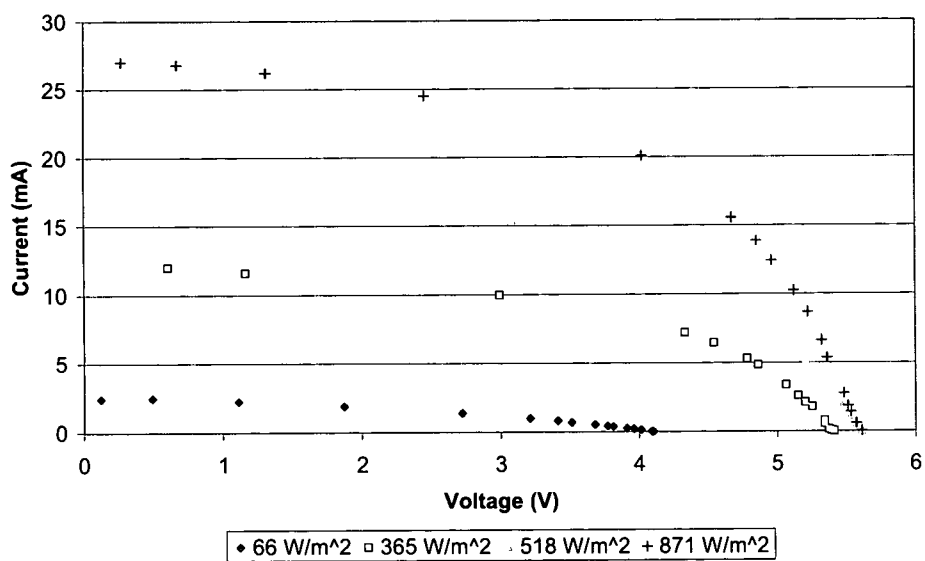


Figure B.2: Solar Cell Characterization for Powerfilm® SP4.2-37 on May 24th

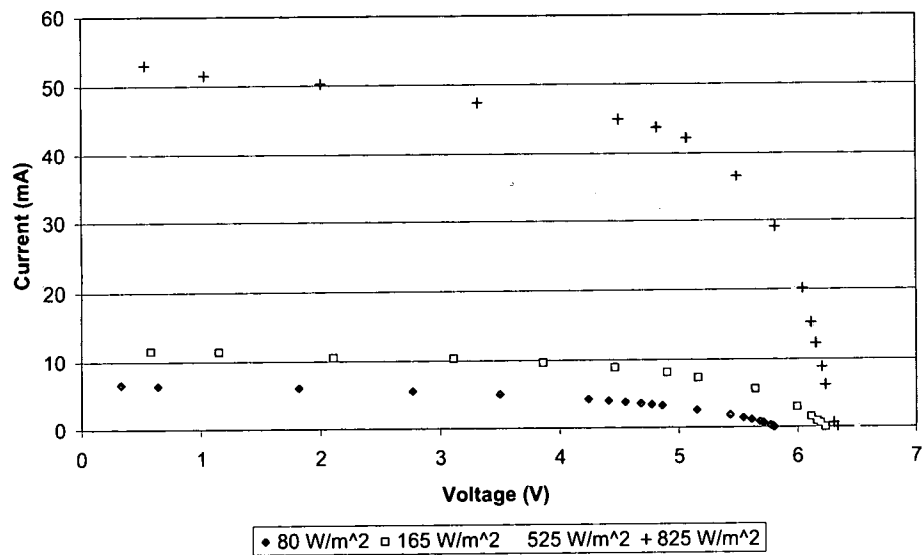


Figure B.3: Solar Cell Characterization for Powerfilm® MPT4.8-75 on May 24th

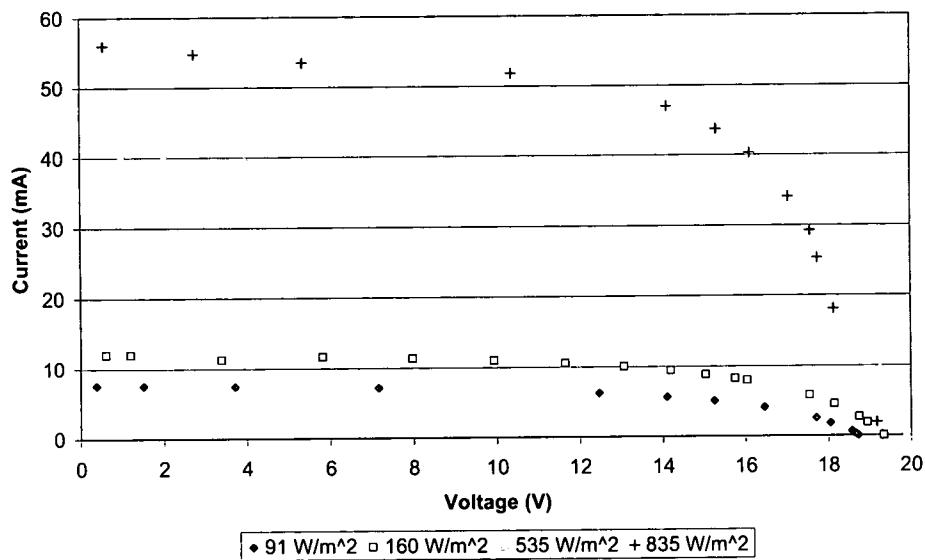


Figure B.4: Solar Cell Characterization for Powerfilm® MPT15-75 on May 24th

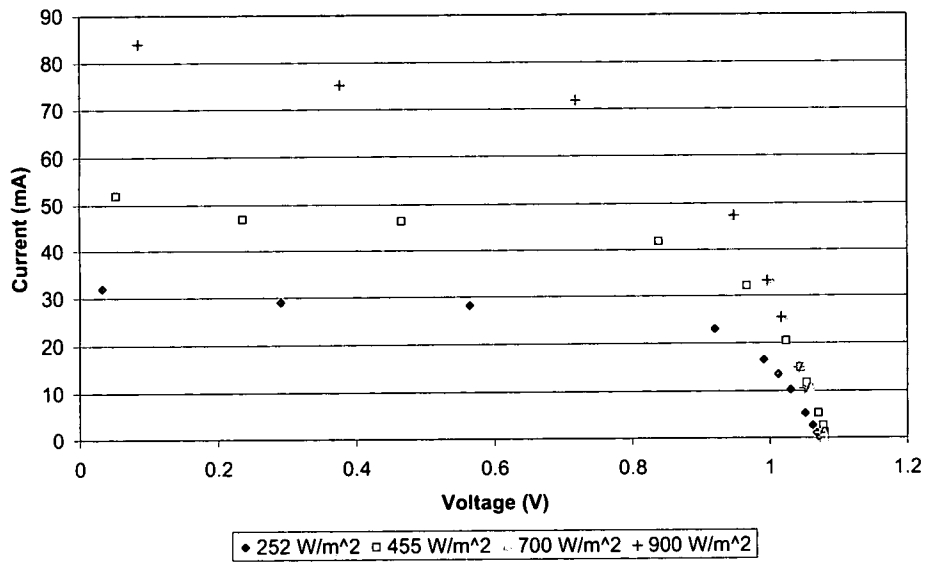


Figure B.5: "Super Cell" Monocrystalline Solar Cell Characterization from June 12th

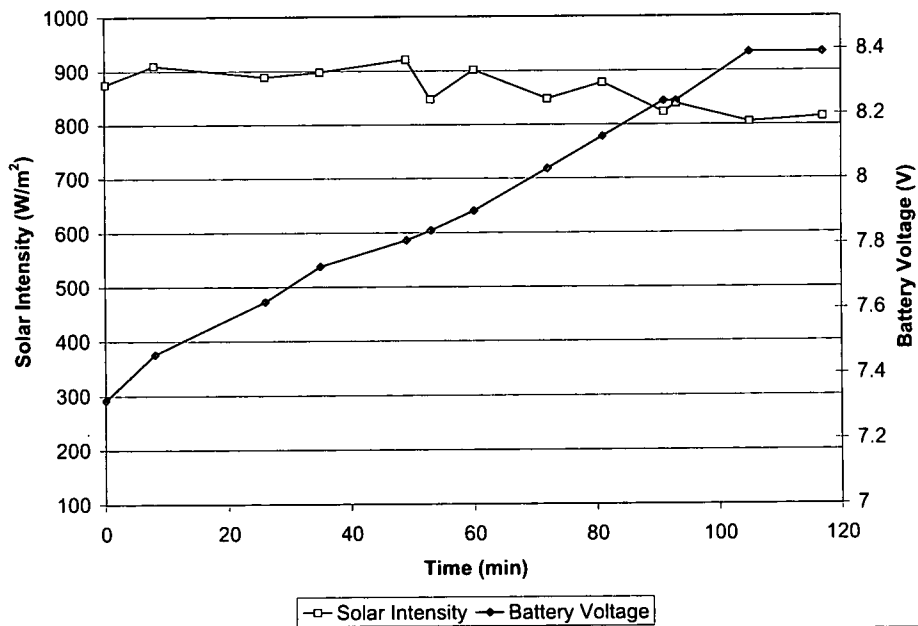


Figure B.6: Battery Charging Test Started at 1:15 p.m. on July 9th

Bibliography

- [1] Grasmeyer, J. M. and Keennon, M. T., "Development of the Black Widow Micro Air Vehicle," No. AIAA-2001-0127, AIAA, 2001.
- [2] Goetzberger, A. and Hoffmann, V., Photovoltaic Solar Energy Generation, Springer, Germany, 2005.
- [3] Patel, M. R., Wind and Solar Power Systems: Design, Analysis, and Operation, CRC Press - Taylor and Francis Group, Boca Raton, FL, 2nd ed., 2006.
- [4] Nelson, J., The Physics of Solar Cells, Imperial College Press, London, England, 2003.
- [5] Leo, D. J., Engineering Analysis of Smart Material Systems, John Wiley and Sons, 2007.
- [6] Maxim Integrated Products, Sunnyvale, CA, MAX745 Evaluation Kit, September 2003.
- [7] Cochran, J., "Beginning of RC," <http://jimsr.com/good-information.html>, 2007.
- [8] Arthur F. Huber, Lt Col, U., "Death By a Thousand Cuts: Micro-Air Vehicles (MAV in the Service of Air Force Missions," Tech. rep., Air War College, Air University, April 2001.
- [9] Tiron, R., "Army Unmanned Air Vehicles Proliferate in the Battlefield," National Defense, May 2004.
- [10] Jordan, H., "AFRL Tests Unmanned Air Vehicle in Urban Terrain," news@afri, December 2006.
- [11] "Windmill," The Columbia Encyclopedia, Columbia University Press 2007, Sixth Edition.
- [12] Nishida, T., Lin, J., Hgo, K., Ren, F., Norton, D., Pearton, S., Cattafesta, L., Sheplak, M., Jun, J., Kasyap, A., Johnson, D., and Phipps, A., "Wireless Hydrogen Sensor Self-Powered Using Ambient Vibration and Light," ASME International Mechanical Engineering Congress and Exposition, ASME, November 5-10 2006.

- [13] Robbins, W. P., Morris, D., Marusic, I., and Novak, T. O., "Wind-Generated Electrical Energy Using Flexible Piezoelectric Materials," ASME, Nov 5-10 2006.
- [14] Rowe, D., "Thermoelectrics, An Environmentally-Friendly Source of Electrical Power," Renewable Energy, Vol. 16, 1999, pp. 1251–1256.
- [15] Aldous, S., "How Solar Cells Work," [http : //science.howstuffworks.com/solar – cell.htm](http://science.howstuffworks.com/solar-cell.htm), April 1 2000.
- [16] Partain, L. D., editor, Solar Cells and Their Applications, John Wiley and Sons, Inc., New York, NY, 1995.
- [17] Dornheim, M. A., "Perpetual Motion," Aviation Week, June 27 2005, pp. 48–52.
- [18] "NASA Helios Fact Sheet," [http : //www.nasa.gov/centers/dryden/news/FactSheets/](http://www.nasa.gov/centers/dryden/news/FactSheets/), July 2006.
- [19] Gautschi, G., Piezoelectric Sensorics, Springer-Verlag, Germany, 2002.
- [20] Roundy, S. and Wright, P. K., "A Piezoelectric Vibration Based Generator for Wireless Electronics," Smart Materials and Structures, Vol. 13, August 2004, pp. 1131–1142.
- [21] Glynn-Jones, P., Beeby, S., and White, N., "Towards a Piezoelectric Vibration-Powered Microgenerator," IEE Proc.-Sci. Meas. Technol., Vol. 148, IEE, March 2001, pp. 68–72.
- [22] Tieck, R., Carman, G., and Lee, D. E., "Electrical Energy Harvesting Using a Mechanical Rectification Approach," IMECE2006-15712, ASME, 2006.
- [23] Sodano, H. A., Park, G., Leo, D. J., and Inman, D. J., "Use of Piezoelectric Energy Harvesting Devices for Charging Batteries," Smart Structures and Materials, edited by D. Inaudi and E. Udd, Vol. 5050, SPIE, 2003, pp. 101–108.
- [24] Sodano, H. A., Lloyd, J., and Inman, D. J., "An Experimental Comparison Between Several Active Composite Actuators for Power Generation," .
- [25] Sodano, H. A., Inman, D. J., and Park, G., "Comparison of Piezoelectric Energy Harvesting Devices for Recharging Batteries," Journal of Intelligent Material Systems and Structures, Vol. 16, October 2005, pp. 799–807.
- [26] Leon, R. A., Pina, C. A., Ynilmez, A., Tansel, I. N., Pereira, C. M., and Roth, L. E., "Development of a Small Energy Scavenger," Florida Conference on Recent Advances in Robotics, May 25-26 2006.
- [27] Lal, A., Duggirala, R., and Li, H., "Pervasive Power: A Radioisotope-Powered Piezoelectric Generator," Energy Harvesting and Conservation, Jan-Mar 2005, pp. 53–61.
- [28] Badel, A., Guyomar, D., Lefeuvre, E., and Richard, C., "Piezoelectric Energy Harvesting using a Synchronized Switch Technique," Journal of Intelligent Material Systems and Structures, Vol. 17, August-September 2006, pp. 831–839.

- [29] Ottman, G. K., Hofmann, H. F., Bhatt, A. C., and Lesieutre, G. A., "Adaptive Piezoelectric Energy Harvesting Circuit for Wireless Remote Power Supply," IEEE Transactions on Power Electronics, Vol. 17, No. 5, September 2002, pp. 669–676.
- [30] Guan, M. and Liao, W.-H., "Efficiency of a Piezoelectric Energy Harvesting Circuit for Rechargeable Batteries," .
- [31] Ottman, G. K., Hofmann, H. F., and Lesieutre, G. A., "Optimized Piezoelectric Energy Harvesting Circuit Using Step-Down Converter in Discontinuous Conduction Mode," IEEE Transactions on Power Electronics, Vol. 18, No. 2, March 2003, pp. 696–703.
- [32] Charneie, D., Mo, C., Frederick, A. A., and W.Clark, W., "Tunable Piezoelectric Cantilever Beams for Energy Harvesting," ASME, November 5-10 2006.
- [33] Han, J., von Jouanne, A., Le, T., Mayaram, K., and Fiez, T., "Novel Power Conditioning Circuits for Piezoelectric Micro Power Generators," 2004, pp. 1541–1546.
- [34] Ngo, K. D. T., Phipps, A., and Nishida, T., "Power Converters for Piezoelectric Energy Extraction," ASME, Nov 5-10 2006.
- [35] Hallinan, K. P., Sanders, B., Somphone, T., and Ephrem, G., "Entropy Generation Metric for Evaluating, Optimizing and Forecasting Aircraft Energy Management Systems," International Journal of Exergy, Vol. 2, No. 2, 2005, pp. 120–145.
- [36] Rutowski, E. S., "Energy Approach to the General Aircraft Performance Problem," Aerodynamics Session, Annual Summer Meeting, IAS, Los Angeles, IAS, July 15-17 1953, pp. 187–195.
- [37] Bejan, A., "A Role for Exergy Analysis and Optimization in Aircraft Energy-System Design," ASME International Mechanical Engineering Congress and Exposition, Nashville, Tennessee, ASME, November 14-19 1999.
- [38] Niedzballa, H. and Schmitt, D., "Comparison of the Specific Energy Demand of Aeroplanes and Other Vehicle Systmes," Aircraft Design 4, 2001, pp. 163–178.
- [39] Figliola, R., Tipton, R., and Li, H., "Exergy Approach to Decision-Based Design of Integrated Aircraft Thermal Systems," Journal of Aircraft, Vol. 40, No. 1, January-February 2003, pp. 49–55.
- [40] Roth, B., "The Role of Thermodynamic Work Potential in Aerospace Vehicle Design," No. ISABE 2003-1200, AIAA, 2003.
- [41] Ahlers, K., Hallinan, K., Sanders, B., and McCarty, R., "Design of a Multifunctional Aircraft Skin with Energy Harvesting via Entropy Generation Minimization," ASME, Nov 5-10 2006.
- [42] Butt, J., A Study of Morphing Wing Effectiveness in Fighter Aircraft using Exergy Analysis and Global Optimization Techniques, Master's thesis, Virginia Polytechnic Institute and State University, December 2005.

R002S93390

- [43] Cengel, Y. A. and Boles, M. A., Thermodynamics, An Engineering Approach, McGraw-Hill, Boston, 6th ed., 2008.
- [44] Smith, R. J., Circuits, Devices, and Systems, John Wiley and Sons, 3rd ed., 1976.
- [45] Raymer, D. P., Aircraft Design: A Conceptual Approach, American Institute of Aeronautics and Astronautics, Inc, Reston, VA, 3rd ed., 1999.
- [46] "Product Details," [http : //www.powerfilmsolar.com/products/oemcomponents/index.htm](http://www.powerfilmsolar.com/products/oemcomponents/index.htm), 2006.
- [47] Sodano, H., Park, G., and Inman, D., "Estimation of Electric Charge Output for Piezo-electric Energy Harvesting," Journal of Strain, Vol. 40, No. 2, 2004, pp. 49–58.
- [48] Meirovitch, L., Elements of Vibration Analysis, McGraw-Hill, Inc., 2nd ed., 1986.
- [49] Piezo Systems, Inc., 186 Massachusetts Ave Cambridge, MA 02139, Catalog #7, 7th ed., 2005.
- [50] Roundy, S., "On the Effectiveness of Vibration-Based Energy Harvesting," Journal of Intelligent Material Systems and Structures, Vol. 16, October 2005, pp. 809–823.